

A thermodynamic framework for modelling membrane transporters

Michael Pan^a, Peter J. Gawthrop^a, Kenneth Tran^b, Joseph Cursons^{c,d},
Edmund J. Crampin^{a,e,f,*}

^a*Systems Biology Laboratory, School of Mathematics and Statistics, and Department of Biomedical Engineering, Melbourne School of Engineering, University of Melbourne, Parkville, Victoria 3010, Australia*

^b*Auckland Bioengineering Institute, University of Auckland*

^c*Bioinformatics Division, Walter and Eliza Hall Institute of Medical Research, Parkville, Victoria 3052, Australia*

^d*Department of Medical Biology, School of Medicine, University of Melbourne, Parkville, Victoria 3010, Australia*

^e*School of Medicine, Faculty of Medicine, Dentistry and Health Sciences, University of Melbourne, Parkville, Victoria 3010*

^f*ARC Centre of Excellence in Convergent Bio-Nano Science and Technology, Melbourne School of Engineering, University of Melbourne, Parkville, Victoria 3010, Australia*

Abstract

Membrane transporters contribute to the regulation of the internal environment of cells by translocating substrates across cell membranes. Like all physical systems, the behaviour of membrane transporters is constrained by the laws of thermodynamics. However, many mathematical models of transporters, especially those incorporated into whole-cell models, are not thermodynamically consistent, leading to unrealistic behaviour. In this paper we use a physics-based modelling framework, in which the transfer of energy is explicitly accounted for, to develop thermodynamically consistent models of transporters. We then apply this methodology to model two specific transporters: the cardiac sarcoplasmic/endoplasmic Ca^{2+} ATPase (SERCA) and the cardiac Na^+/K^+ ATPase.

Keywords: bond graph, biochemistry, chemical reaction network, biomedical engineering, systems biology

1. Introduction

The cell membrane is a physical barrier that separates the internal environment of a cell from its external environment, as well as many compartments within the cell. By transporting chemical species across the membrane, the cell regulates concentration within each compartment, providing the environment necessary for many cellular processes ([Keener](#)

*Corresponding author

Email addresses: panm@student.unimelb.edu.au (Michael Pan), peter.gawthrop@unimelb.edu.au (Peter J. Gawthrop), k.tran@auckland.ac.nz (Kenneth Tran), cursons.j@wehi.edu.au (Joseph Cursons), edmund.crampin@unimelb.edu.au (Edmund J. Crampin)

and Sneyd, 2009). A key contributor to these transport systems are membrane transporters, which are proteins located in cell membranes that maintain cell volume (Glitsch, 2001), set up ionic gradients required for electrical (Glitsch, 2001) and calcium signalling (Periasamy and Kalyanasundaram, 2007; Blaustein and Lederer, 1999), and transport sources of energy into the cell (Mueckler and Thorens, 2013). As with all physical processes, transporters must comply with the principles of thermodynamics (Oster et al., 1973; Hwang, 2004; Beard and Qian, 2008). Because each chemical species within a solution is associated with a chemical potential that increases with concentration, passive transporters can only move substrates from a region of high concentration to a region of low concentration (Keener and Sneyd, 2009; Beard and Qian, 2008). To move a substrate against a concentration gradient, a source of energy must be provided. For example, active transporters use ATP hydrolysis to drive the transport of substrates against a potential gradient (Keener and Sneyd, 2009).

Mathematical models of membrane transporters have been developed for the purpose of understanding their transport mechanism, and predicting their behaviour beyond experimental measurements. However, despite the wealth of models available for transporters, thermodynamic consistency has not usually been applied. As a result, many of these models describe physically infeasible systems where for example, species are transported against their potential gradients in the absence of an energy source, therefore generating energy out of nowhere. In the current literature, thermodynamic consistency is commonly violated through the use of equations that describe irreversible transporters, neglect dependence on certain metabolites, or have incorrect equilibrium points (Gawthrop and Crampin, 2014; Smith and Crampin, 2004; Tran et al., 2009). While there are methods for incorporating thermodynamic constraints such as detailed balance (Liebermeister et al., 2010; Beard and Qian, 2008; Smith and Crampin, 2004) and the Nernst potential (Keener and Sneyd, 2009), they tend to be scattered around the literature, and are not universally applied. Furthermore, many transporters are electrogenic, therefore there is an interaction between chemical and electrical potential (Smith and Crampin, 2004; Terkildsen et al., 2007), and the multidomain nature of these transporters can confound efforts to develop thermodynamically consistent models. In some cases, thermodynamic inconsistency may impact on the ability of a model to remain physiological under a wide range of conditions. For example, in the context of heart failure, where ATP is depleted, active transporters such as the Na^+/K^+ ATPase and sarcoplasmic/endoplasmic Ca^{2+} ATPase (SERCA) operate at reduced rates. Whole cell models of cardiac cells generally do not describe this metabolite dependence because they neglect thermodynamic constraints (Smith and Crampin, 2004), and while thermodynamically consistent models capture these effects (Terkildsen et al., 2007; Tran et al., 2009), they tend to be the exception rather than the rule.

To facilitate the incorporation of thermodynamic constraints into models of membrane transporters, we require a framework that is (a) thermodynamically consistent by design; (b) able to reproduce known thermodynamic constraints; and (c) general enough to model a wide range of transporters. We propose the use of bond graphs, which are a physics-based framework in which energy transfer is explicitly modelled through connections between physical components, therefore satisfying thermodynamic consistency (Gawthrop and Smith, 1996; Borutzky, 2010). The bond graph representation is also domain-independent, therefore

it is general enough to represent a wide range of physical systems. Bond graphs were originally invented by Henry Paynter for use in hydroelectric systems (Paynter, 1961), but they also naturally represent electrical and mechanical systems (Borutzky, 2010). The reader is referred to the texts by Gawthrop and Smith (1996), Borutzky (2010) and Gawthrop and Bevan (2007) for a comprehensive introduction to bond graph theory. More recently, bond graphs have been extended to chemical (Thoma and Bouamama, 2000), biochemical (Oster et al., 1973; Gawthrop and Crampin, 2014) and electrochemical systems (Gawthrop, 2017), enabling bond graph modelling of membrane transporters such as the sodium-glucose transport protein 1 (SGLT1) (Gawthrop and Crampin, 2017). Models of electrogenic membrane transporters have recently been incorporated into a bond graph model of cardiac electrophysiology (Pan et al., 2018a). A further advantage of modelling transporters as bond graphs is that they are modular, therefore individual models of transporters are easily coupled to other bond graph models to build comprehensive models of biological systems (Gawthrop et al., 2015).

In this paper, we review the bond graph theory required for modelling ion transporters and use bond graphs to build simple hypothetical models of transporters (Section 2), demonstrating that bond graphs capture important thermodynamic concepts such as detailed balance, free energy of reaction and the Nernst potential. We then develop a bond graph model of cardiac SERCA based on existing work by Tran et al. (2009), and used the bond graph model to assess energy consumption and efficiency (§ 3.1). Bond graphs also provide a framework for detecting thermodynamic inconsistencies within existing models. In § 3.2 we develop a new model of Na⁺/K⁺ ATPase based on existing work by Terkildsen et al. (2007), and verify that the model complies with thermodynamic constraints. These examples illustrate that bond graphs are a unifying framework for accounting for thermodynamic constraints in models of membrane transporters. We believe that the bond graph approach will prove to be a powerful tool in the development of thermodynamically consistent models of transporters, and other cellular processes in which energy transduction plays an important role.

2. Hypothetical models

2.1. Enzyme cycle

In biochemical systems, Gibbs free energy (also called Gibbs energy or free energy) is transmitted between species and reactions (Atkins and De Paula, 2006). Like all physical systems, biochemical systems must comply with the laws of thermodynamics, therefore reactions can only proceed in the direction of decreasing chemical potential. However, chemical potential is ignored by many existing models, often resulting in physically unrealistic behaviour (Gawthrop and Crampin, 2014; Gawthrop et al., 2015). Bond graphs account for chemical potential by decomposing the transfer of power into a product of chemical potential (μ [J/mol]) and molar flow rate (v [mol/s]) (Gawthrop and Crampin, 2014). Power is transmitted between components within a bond graph by connecting them with bonds that carry chemical potential and molar flow rate. Because the power leaving one component is transmitted to another, bond graphs are thermodynamically consistent, that is, the flow of energy is explicitly accounted for. In bond graph terminology, chemical potential is known

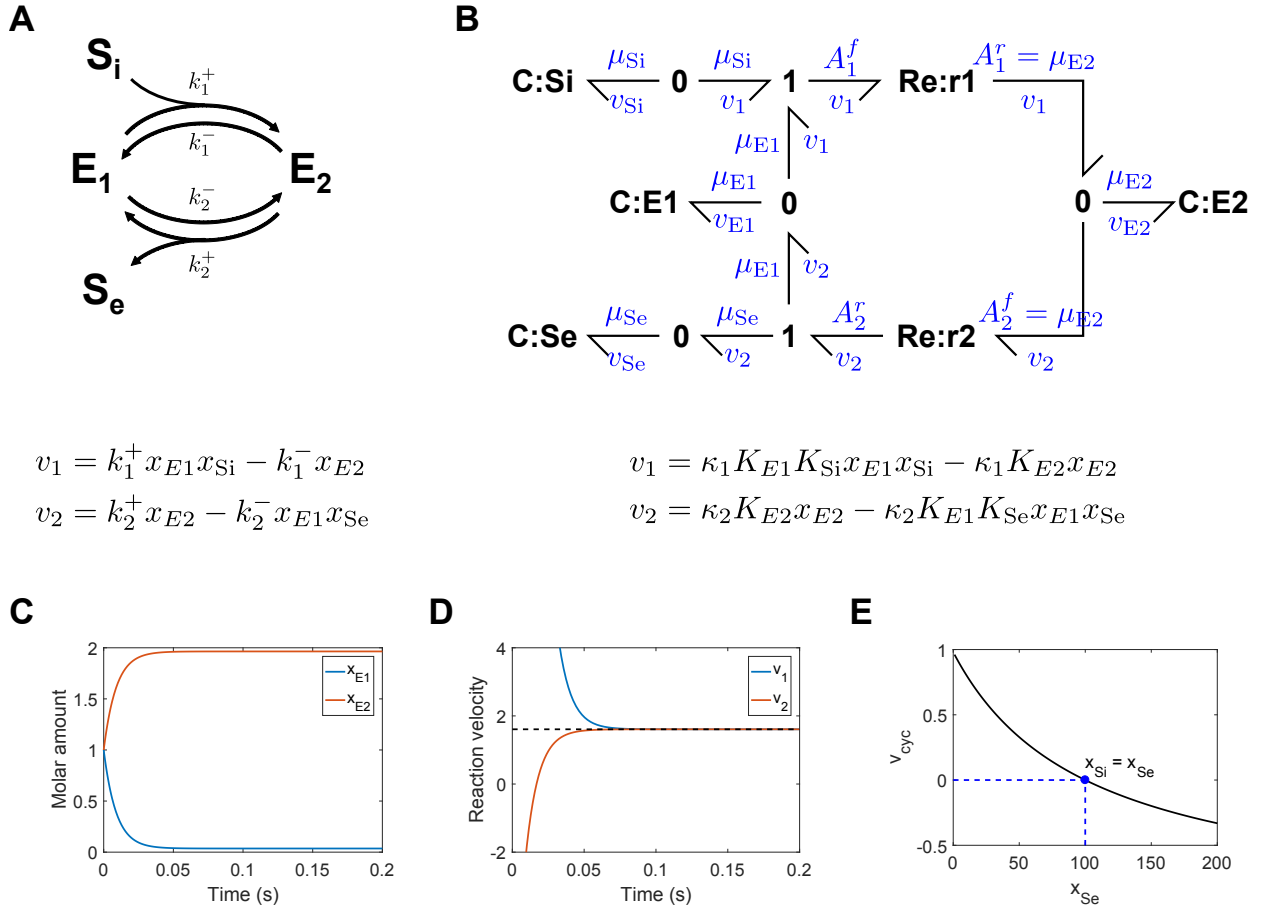


Figure 1: A simple enzyme cycle. (A) Kinetic model; (B) Bond graph model. S_i and S_e are the intracellular and extracellular substrate respectively, E_1 is the unbound transporter, and E_2 is the transporter bound to substrate. A simulation was run with unity parameters, the initial conditions $x_{E1} = x_{E2} = 1$ and $x_{Si} = 100$ and $x_{Se} = 10$. The resulting molar amounts of transporter states (C) and reaction velocities (D) were plotted against time. (E) Using $x_{Si} = 100$, the steady-state cycling rates were plotted against x_{Se} , with the blue dot indicating the equilibrium point.

as the effort variable, and molar flow rate is known as the flow variable (Gawthrop and Crampin, 2014).

In this section, we use a simple transporter model to outline the essential aspects of modelling biochemical systems using bond graphs (Figure 1A). This transporter model contains a two-state enzyme cycle, where an uncharged substrate S binds to the enzyme on the intracellular (i) side, and unbinds on the extracellular (e) side. We denote the substrate in a specific compartment as S_x , where $x \in \{i, e\}$. The kinetic model is shown in Figure 1A, and the bond graph representation of this reaction cycle is shown in Figure 1B. Because a thermodynamic approach implies reversibility for all reactions (Polettini and Esposito, 2014; Gawthrop and Crampin, 2014), the transport of the substrate can proceed in both directions, depending on the direction of the chemical gradient.

Chemical energy is stored within the species of a biochemical system (Atkins and De Paula, 2006). This energy allows the system to do work through chemical reactions. The ability of a species s to drive a reaction is given by the chemical potential μ_s [J/mol], which is dependent on the molar amount of species x_s [mol] in a logarithmic manner (Keener and Sneyd, 2009; Atkins and De Paula, 2006):

$$\mu_s = RT \ln(K_s x_s) \quad (1)$$

where $R = 8.314$ J/K/mol is the ideal gas constant, T [K] is the absolute temperature and K_s [mol⁻¹] is the species thermodynamic constant. Therefore, the chemical potentials of the species in the enzyme cycle are

$$\mu_{S_i} = RT \ln(K_{S_i} x_{S_i}) \quad (2)$$

$$\mu_{S_e} = RT \ln(K_{S_e} x_{S_e}) \quad (3)$$

$$\mu_{E_1} = RT \ln(K_{E_1} x_{E_1}) \quad (4)$$

$$\mu_{E_2} = RT \ln(K_{E_2} x_{E_2}) \quad (5)$$

Because species store energy, they are represented as **C** components in the bond graph model (Figure 1B), as they are analogous to capacitors in electrical circuits.

The chemical energy stored within the various species of a biochemical system is used to drive reactions, which convert chemical species into other chemical species, dissipating chemical energy in the process. The rate of reaction can be related to the chemical potential of its reactants and products using the Marcelin-de Donder equation (Gawthrop and Bevan, 2007; Oster et al., 1973):

$$v_R = \kappa_R (e^{A_R^f/RT} - e^{A_R^r/RT}) \quad (6)$$

where for a reaction R , v_R [mol/s] is the rate of reaction, κ_R [mol/s] is the reaction rate constant, A_R^f [J/mol] is the forward affinity (representing the total chemical potential of the reactants) and A_R^r [J/mol] is the reverse affinity (representing the total chemical potential of the products). For the enzyme cycle example in Figure 1B, the reaction rates of the upper

and lower reactions are given by the equations

$$v_1 = \kappa_1(e^{A_1^f/RT} - e^{A_1^r/RT}) \quad (7)$$

$$v_2 = \kappa_2(e^{A_2^f/RT} - e^{A_2^r/RT}) \quad (8)$$

As seen in [Figure 1B](#), reactions are represented as **Re** components in bond graph modelling.

In the enzyme cycle, some species are involved in more than one reaction. Therefore we require constraints to ensure that (a) the same chemical potential is used for the involvement of the same species in different reactions and (b) the contributions of each reaction are summed when calculating the rate of change of each species. These constraints are captured by the **0** junction in bond graph modelling, which accounts for the first constraint by setting the chemical potentials of all connected bonds to be equal. In [Figure 1B](#), there are four **0** junctions corresponding to each species. The second constraint is captured through the conservation equations

$$v_{Si} = -v_1 \quad (9)$$

$$v_{Se} = v_2 \quad (10)$$

$$v_{E1} = v_2 - v_1 \quad (11)$$

$$v_{E2} = v_1 - v_2 \quad (12)$$

0 junctions are analogous to parallel connections in electric circuits, and the Eqs. 9–12 represent the biochemical version of Kirchhoff’s current law. Note that the molar flow rates of the bonds connecting to each **0** junction sum to zero, therefore the **0** junction conserves power ([Borutzky, 2010](#)).

In this example, both reactions involve the combination or dissociation of chemical species, and therefore have multiple reactants or products. To account for this, we require constraints so that (a) the rate at which each species is produced/consumed by the reaction is equal to the rate of reaction and (b) the affinities of each reaction are the totals of the chemical potentials of the reactants or products. These constraints are captured by **1** junctions in bond graph modelling, which satisfy the first constraint by fixing the molar flow rates of each connected bond to equal values. In [Figure 1B](#), there are two **1** junctions representing the association and dissociation of substrate. The second constraint is accounted for through the conservation laws

$$A_1^f = \mu_{Si} + \mu_{E1} \quad (13)$$

$$A_2^r = \mu_{Se} + \mu_{E1} \quad (14)$$

1 junctions are analogous to series connections in electric circuits, and Eqs. 13–14 are biochemical versions of Kirchhoff’s voltage law. Note that since the chemical potentials of all bonds connected to **1** junctions sum to zero, they are power conserving, like the **0** junction ([Borutzky, 2010](#)).

Using the components described above, it is possible to derive a differential equation for

the enzyme cycle. By substituting Eqs. 13–14 into Eqs. 7–8, we find that the reaction rates are

$$v_1 = \kappa_1(e^{(\mu_{S_i} + \mu_{E_1})/RT} - e^{\mu_{E_2}/RT}) = \kappa_1 K_{S_i} K_{E_1} x_{S_i} x_{E_1} - \kappa_1 K_{E_2} x_{E_2} \quad (15)$$

$$v_2 = \kappa_2(e^{\mu_{E_2}/RT} - e^{(\mu_{S_e} + \mu_{E_1})/RT}) = \kappa_2 K_{E_2} x_{E_2} - \kappa_2 K_{S_e} K_{E_1} x_{S_e} x_{E_1} \quad (16)$$

Hence the bond graph components are able to reproduce the mass action equations, with the kinetic parameters

$$k_1^+ = \kappa_1 K_{E_1} K_{S_i} \quad (17)$$

$$k_1^- = \kappa_1 K_{E_2} \quad (18)$$

$$k_2^+ = \kappa_2 K_{E_2} \quad (19)$$

$$k_2^- = \kappa_2 K_{E_1} K_{S_e} \quad (20)$$

By using the conservation laws from Eqs. 9–12, the rates of change for each species are

$$\begin{aligned} \dot{x}_{S_i} &= v_{S_i} = -v_1 \\ &= -k_1^+ x_{S_i} x_{E_1} + k_1^- x_{E_2} \end{aligned} \quad (21)$$

$$\begin{aligned} \dot{x}_{S_e} &= v_{S_e} = v_2 \\ &= k_2^+ x_{E_2} - k_2^- x_{S_e} x_{E_1} \end{aligned} \quad (22)$$

$$\begin{aligned} \dot{x}_{E_1} &= v_{E_1} = v_2 - v_1 \\ &= -k_1^+ x_{S_i} x_{E_1} + k_1^- x_{E_2} + k_2^+ x_{E_2} - k_2^- x_{S_e} x_{E_1} \end{aligned} \quad (23)$$

$$\begin{aligned} \dot{x}_{E_2} &= v_{E_2} = v_1 - v_2 \\ &= k_1^+ x_{S_i} x_{E_1} - k_1^- x_{E_2} - k_2^+ x_{E_2} + k_2^- x_{S_e} x_{E_1} \end{aligned} \quad (24)$$

The above equations are applicable to an isolated system. However, since transporters are dissipative systems, i.e. they release energy as heat, it is impossible for these to operate continuously at steady state without an external power supply. Therefore, we model these external power supplies by holding certain species at constant concentrations rather than allowing them to dynamically vary. Such species are known as chemostats (Poletini and Esposito, 2014). In this example, we assume that the concentrations of the substrates S_i and S_e are constant, so that Eqs. 21 and 22 are replaced by

$$\dot{x}_{S_i} = 0 \quad (25)$$

$$\dot{x}_{S_e} = 0 \quad (26)$$

Because an external flow of species is required to keep the concentration of the species constant, chemostats are not energy conserving, but rather represent the influx or release of energy into the external environment. Thus chemostats turn a biochemical system from an isolated system into an open system that communicates with its external environment, and can therefore be used to couple models together. In bond graph modelling, \mathbf{C} components

are replaced with **Se** (effort source) components when they become chemostats to indicate the transfer of power with an external source. Since species can be represented using **C** or **Se** components interchangeably depending on the purpose of the model (Gawthrop et al., 2017; Gawthrop, 2017), we represent species as **C** components in all diagrams within this paper, and mention in text whether certain species are treated as “chemostats” in the analysis.

For the remainder of Section 2, we assume that:

1. Apart from the states of the transporter (e.g. E_1, E_2), the concentrations of all species are constant (i.e. they are modelled as chemostats).
2. The volumes of all compartments are equal, so that the amount of each species directly corresponds to concentration. In real biological systems, compartments will have different volumes, and we show how to incorporate these effects in Appendix B of the Supplementary Material.
3. The parameters K and κ for each species and reaction take on unity values.

Assumptions 2 and 3 are made to simplify the analysis in this section, although we show how to generalise beyond these assumptions in later sections.

Figure 1C,D shows simulations of this model when the amount of enzyme is small relative to the amount of substrate, thus we expect the system to achieve a steady state relatively quickly. At steady state, the amounts of each pump state are constant, and the two reaction velocities converge towards the same value, as dictated by the pathway analysis of Gawthrop and Crampin (2017). We are often interested in the cycling (or turnover) rate at steady state, v_{cyc} , which is given by $v_{\text{cyc}} = V/e_0$, where V is the steady-state reaction rate, and $e_0 = x_{E1} + x_{E2}$ is the total amount of transporter (Atkins and De Paula, 2006).

Figure 1E shows the effect of changing x_{Se} on cycling rate, indicating an inverse relationship: as x_{Se} increases, the transporter operates at a lower rate, and eventually operates in the reverse direction as expected. The bond graph model captures the fundamental physical constraint that the equilibrium point between the forward and reverse regimes of operation occurs when $x_{\text{Se}} = x_{\text{Si}}$. Therefore the simple transporter can only allow transport of its substrate down its concentration gradient.

The direction in which each reaction proceeds is determined by the Gibbs free energy of reaction ΔG . Because reactions can only run in the direction of decreasing chemical potential, they will only proceed in the forward direction if ΔG is negative. The Gibbs free energy of reaction relates to the affinities $A = A^f - A^r$ of the **Re** components in bond graph models. Since efforts in the biochemical domain are associated with Gibbs free energy, the Gibbs free energy of reaction is the negative of affinity:

$$\Delta G = -A = A^r - A^f \quad (27)$$

Therefore, the free energies of each of the reactions in this example are

$$\Delta G_1 = \mu_{E2} - \mu_{E1} - \mu_{\text{Si}} \quad (28)$$

$$\Delta G_2 = \mu_{E1} + \mu_{\text{Se}} - \mu_{E2} \quad (29)$$

At steady state, the transporter’s direction of operation is determined by the Gibbs free energy of the overall reaction $S_i \rightleftharpoons S_e$, which is also the sum of all reactions in its cycle (Gawthrop and Crampin, 2017):

$$\Delta G = \Delta G_1 + \Delta G_2 = \mu_{S_e} - \mu_{S_i} \quad (30)$$

By substituting Eq. 1 and setting $\Delta G = 0$, the equilibrium of the system can be found:

$$\Delta G = RT \ln(K_{S_e} x_{S_e}) - RT \ln(K_{S_i} x_{S_i}) = RT \ln(x_{S_e}/x_{S_i}) = 0 \quad (31)$$

$$\Rightarrow x_{S_e} = x_{S_i} \quad (32)$$

Therefore, as expected, the point at which the free energy is zero corresponds to the equilibrium of the transporter.

To ensure that the equilibrium occurs at $x_{S_e} = x_{S_i}$, we must specify the equilibrium between the substrate in each compartment:

$$K_{S_i}/K_{S_e} = K^{\text{eq}} = 1 \quad (33)$$

which is exactly equivalent to the detailed balance constraint used in kinetic models (Keener and Sneyd, 2009; Smith and Crampin, 2004; Tran et al., 2009):

$$\frac{k_1^+ k_2^+}{k_1^- k_2^-} = 1 \quad (34)$$

(this can be easily checked by substituting Eq. 33 into Eqs. 17–20). Because bond graphs are thermodynamically consistent, the thermodynamic constraint is simpler and more intuitive when compared to that for the kinetic parameters.

2.2. Coupled reactions

In the previous example, we observed that a passive transporter was unable to move a substrate against its concentration gradient. However, many transporters, including active transporters and exchangers, are able to move substrates against their concentration gradients. Such transporters couple the movement of substrate against a concentration gradient to a process that provides sufficient energy to enable transport. In Figure 2A, we show a simple mechanism for coupling together these processes. In addition to binding S_i and unbinding S_e , the transport also binds A and unbinds B , giving rise to the overall reaction



The reaction $A \rightleftharpoons B$ provides energy for the transport of substrate, and may for example represent ATP hydrolysis in active transporters, or the transport of another species down its concentration gradient in exchangers or cotransporters. The bond graph representation of this chemical reaction network is given in Figure 2B.

To achieve the correct equilibrium point, we use the following thermodynamic constraint,

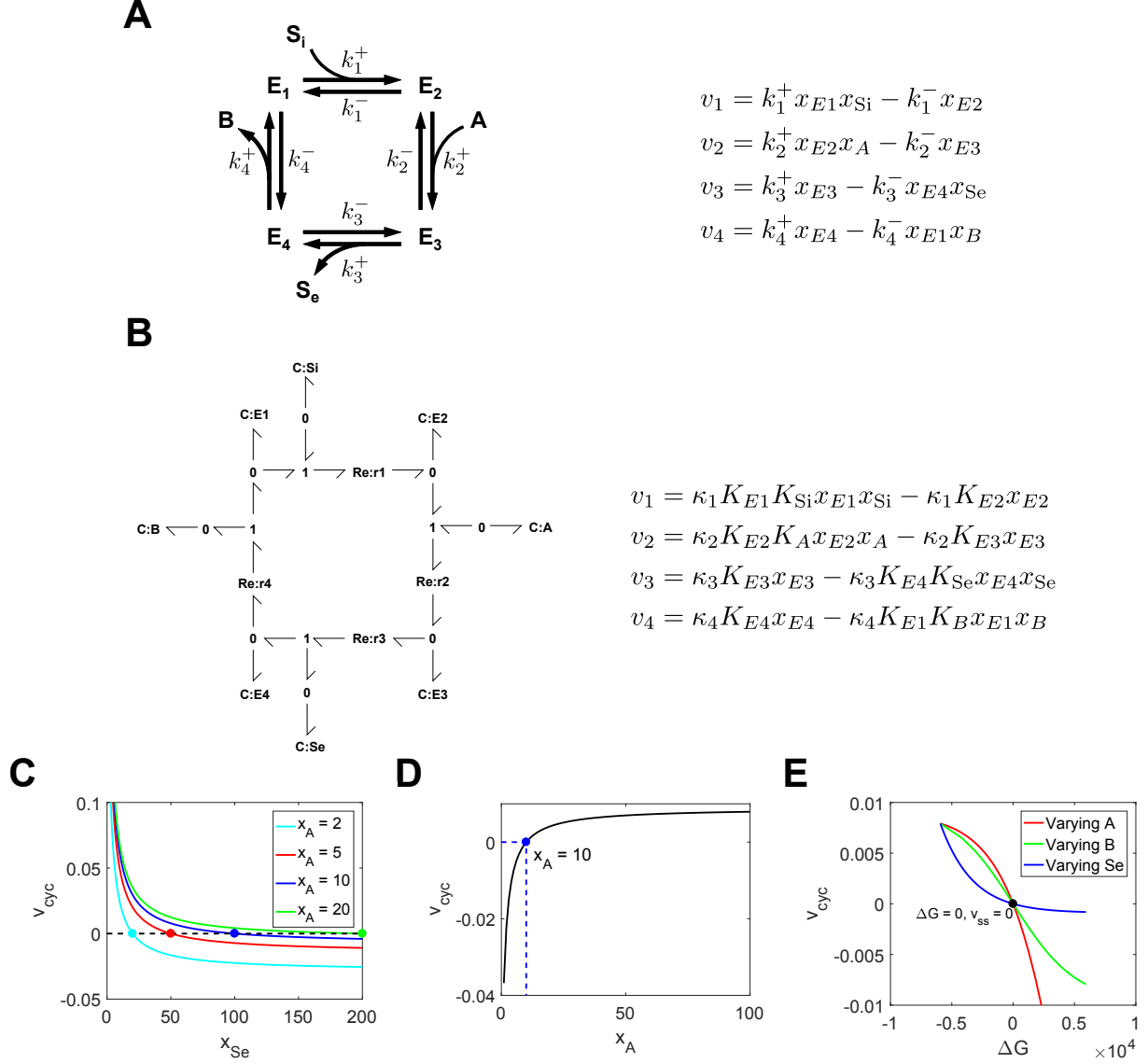


Figure 2: Transport of a species by coupling to an energy supply. (A) Kinetic model; (B) Bond graph model. S_i and S_e are the intracellular and extracellular substrate respectively, A and B are species that provide power for the transport cycle, and E_1 , E_2 , E_3 and E_4 are the transporter states. Simulations were run using the initial conditions $x_{E1} = x_{E2} = x_{E3} = x_{E4} = 0.5$, and chemostats $x_B = 1$, $x_{S_i} = 10$. (C) The effect of x_{S_e} on steady state cycling rate for different x_A . Equilibrium points, where the cycling rates are zero, are denoted by the dots. (D) Effect of x_A on the cycling rate, with $x_{S_e} = 100$. The equilibrium (blue dots) occurs at $x_A = x_{S_e}/(x_{S_i} x_B) = 10$. (E) The relationship between the Gibbs free energy of the transporter and cycling rate, when A , B and S_e are varied.

describing the equilibria between side species:

$$K_{\text{Si}}/K_{\text{Se}} = 1 \quad (36)$$

$$K_A/K_B = 1 \quad (37)$$

Note that K_A/K_B can be set to different values depending on the process that $A \rightleftharpoons B$ represents; it has a value of 1 if it represents the transport of an uncharged substrate (as the equilibrium point occurs when the substrate has the same concentration on either side of the membrane), whereas it is determined by the standard Gibbs free energy of reaction if it represents a reaction such as ATP hydrolysis (see Appendix B of the Supplementary Material).

For a kinetic model with the parameters k_1^+ , k_1^- , k_2^+ , k_2^- , k_3^+ , k_3^- , k_4^+ and k_4^- , the corresponding thermodynamic constraint is

$$\frac{k_1^+ k_2^+ k_3^+ k_4^+}{k_1^- k_2^- k_3^- k_4^-} = \frac{K_{\text{Si}} K_A}{K_{\text{Se}} K_B} = 1 \quad (38)$$

We note here that the thermodynamic constraint between kinetic parameters is more complicated than that in § 2.1 because there are more reactions in the cycle. When the number of reactions in biochemical cycles increases, these thermodynamic constraints become more complex, and harder to derive. By contrast, when bond graph parameters are used, thermodynamic constraints remain simple regardless of cycle complexity, and are more intuitive to formulate.

In Figure 2C we simulated the bond graph model to show the steady-state cycling rates under different values of x_A and x_{Se} . We note that for a passive transporter the equilibrium point occurs at $x_{\text{Se}} = x_{\text{Si}} = 10$, however in this example with $x_A > x_B$, the equilibrium points (represented by dots) occur at $x_{\text{Se}} > x_{\text{Si}}$. With all thermodynamic parameters set to 1, the equilibrium is given by the equation

$$x_{\text{Se}} = x_{\text{Si}} x_A / x_B \quad (39)$$

Thus when $x_A > x_B$ (i.e. the coupled process releases energy), x_{Se} is greater than x_{Si} at equilibrium. Therefore there is a region of operation (when $x_{\text{Si}} < x_{\text{Se}} < x_{\text{Si}} x_A / x_B$) where the transporter can transport S against its concentration gradient. As the value of x_A increases, the equilibrium point shifts towards the right (Figure 2C), indicating that the transporter is able to move S against a greater concentration gradient. This is because with a greater x_A , the reaction $A \rightleftharpoons B$ provides more power, driving the transport in the forward direction (Figure 2D).

The Gibbs free energies of each of the reactions are

$$\Delta G_1 = \mu_{E2} - \mu_{E1} - \mu_{Si} \quad (40)$$

$$\Delta G_2 = \mu_{E3} - \mu_{E2} - \mu_A \quad (41)$$

$$\Delta G_3 = \mu_{E4} + \mu_{Se} - \mu_{E3} \quad (42)$$

$$\Delta G_4 = \mu_{E1} + \mu_B - \mu_{E4} \quad (43)$$

and the free energy of the transporter is

$$\Delta G = \Delta G_1 + \Delta G_2 + \Delta G_3 + \Delta G_4 = \mu_{Se} + \mu_B - \mu_{Si} - \mu_A \quad (44)$$

By substituting Eq. 1 and setting $\Delta G = 0$, we can recover the equilibrium relationship in Eq. 39:

$$\begin{aligned} \Delta G &= RT \ln(K_{Se}x_{Se}) + RT \ln(K_Bx_B) - RT \ln(K_{Si}x_{Si}) - RT \ln(K_Ax_A) \\ &= RT \ln\left(\frac{K_{Se}x_{Se}K_Bx_B}{K_{Si}x_{Si}K_Ax_A}\right) \\ &= RT \ln\left(\frac{x_{Se}x_B}{x_{Si}x_A}\right) = 0 \end{aligned} \quad (45)$$

$$\Rightarrow \frac{x_{Se}x_B}{x_{Si}x_A} = 1 \quad (46)$$

Therefore, the equilibrium for steady-state operation corresponds to the point where the Gibbs free energy of the transport process is zero. We verify this fundamental physical constraint by plotting Gibbs free energy against cycling rate (Figure 2E). We varied the concentrations of A, B and S_e to generate three different curves. Despite differences in the shape of each curve, they each pass through the equilibrium point $\Delta G = 0$, $v_{cyc} = 0$, verifying that the bond graph model correctly captures the relationship between Gibbs free energy and equilibrium. Furthermore, the transporter operates in the forward direction ($v_{cyc} > 0$) with a negative (favourable) Gibbs free energy, and in the reverse direction ($v_{cyc} < 0$) with a positive (unfavourable) free energy.

2.3. Electrogenic transport

Many membrane transporters, including ion exchangers, cotransporters and active ion transporters, move a charged species across a membrane. For those membranes within the cell (such as the plasma membrane, and inner mitochondrial membrane) that are charged, the membrane potential influences both the kinetics and thermodynamics of transport. In this section we explore the impact on transport by modifying the enzyme example in § 2.1, so that the transported substrate has a single unit of positive charge (i.e. $z = 1$) (Figure 3A). For simplicity, we choose to assign the entirety of the electrical dependence to the forward side of the first reaction, which results in an exponential dependence on membrane voltage, arising from thermodynamic constraints (Keener and Sneyd, 2009; Smith and Crampin, 2004).

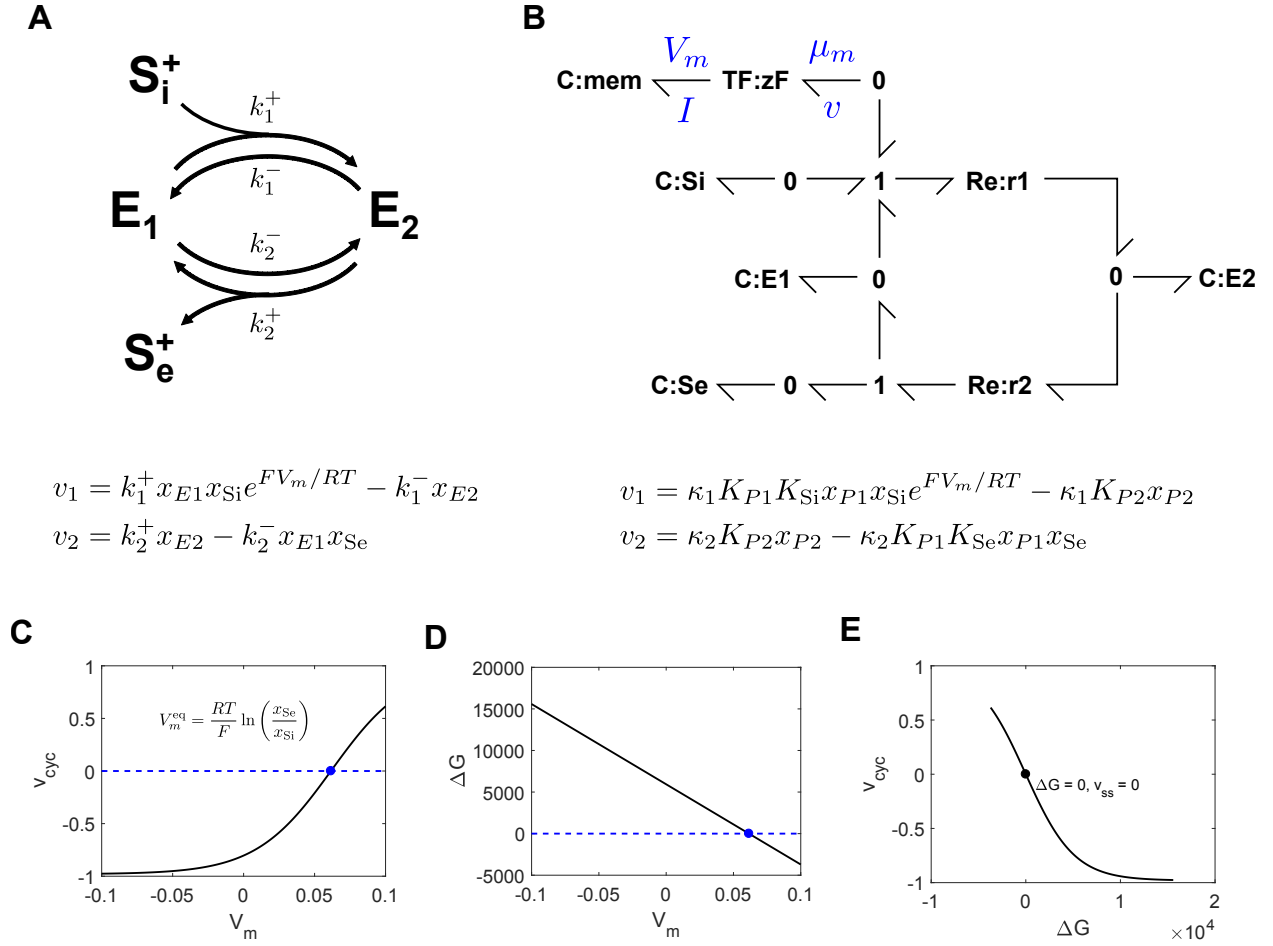


Figure 3: Transport of a charged species (A) Kinetic model; (B) Bond graph model. S_i^+ and S_e^+ are the intracellular and extracellular substrate respectively, E_1 is the unbound transporter, and E_2 is the transporter bound to substrate. Simulations were run with the initial conditions $x_{E1} = x_{E2} = 1$, and chemostats $x_{Si} = 10$, $x_{Se} = 100$. **(C)** Relationship between the membrane potential and cycling rate. The blue dot indicates the equilibrium potential, as predicted by the Nernst equation. **(D)** The effect of membrane potential on the Gibbs free energy of the transporter. **(E)** Relationship between the Gibbs free energy and cycling rate under the simulation conditions, with varying membrane potential.

Because the bond graph representation is domain-independent, physical processes from other physical domains such as electrical or mechanical domains can be modelled by changing the units of the effort and flow variables. In the bond graph model (Figure 3B), the electrical dependence is incorporated by adding a **C** component representing membrane capacitance. This **C** component has similar energy-storage properties to the **C** component for each chemical species, however, in place of Eq. 1, it has a linear constitutive equation $V_m = q_m/C$, where V_m [V] is the membrane potential and q_m [C] is the charge. We use a membrane capacitance of $C = F^2$. Since the capacitor is an electrical component, its power must be converted to chemical power to appropriately describe its influence on reaction kinetics. This conversion is given by Faraday's constant $F = 96485$ C/mol, which relates the membrane potential and current to chemical potential and molar flow rate (Gawthrop et al., 2017):

$$\mu_m = zFV_m \quad (47)$$

$$I = zFv \quad (48)$$

These transformations are described by the **TF** component in Figure 3B. Since $\mu_m v = V_m I$, the **TF** component is a power-conserving transformation.

By substituting the relevant constitutive equations, the rate of reaction 1 is given by

$$v_1 = \kappa_1 (e^{(\mu_{\text{Si}} + \mu_{\text{E1}} + \mu_m)/RT} - e^{\mu_{\text{E2}}/RT}) = \kappa_1 K_{\text{Si}} K_{\text{E1}} x_{\text{Si}} x_{\text{E1}} e^{FV_m/RT} - \kappa_1 K_{\text{E2}} x_{\text{E2}} \quad (49)$$

which corresponds to the exponential dependence of the kinetic reaction scheme. Because adding an electrical component affects the thermodynamics of transport, the equilibrium becomes dependent on membrane potential. As a result, the kinetics of the transporter must depend on membrane voltage to account for changes in equilibrium, although in practice modellers often make assumptions about where the electrical dependence lies due to a lack of experimental data (Smith and Crampin, 2004).

Bond graphs incorporate thermodynamic constraints for electrogenic transport. Because the chemical reaction structure is similar to the system in § 2.1, the constraint in Eq. 33 holds. However, because a single unit of charge is moved across the membrane in a single cycle, there is an additional constraint for charge:

$$z_1^f - z_1^r + z_2^f - z_2^r = z = 1 \quad (50)$$

where z indicates charge, subscripts indicate the reaction number, and superscripts indicate the side of the reaction. In this example, $z_1^f = 1$ and $z_1^r = z_2^f = z_2^r = 0$, therefore Eq. 50 is satisfied.

At equilibrium, the free energy of the overall reaction is zero (Gawthrop and Crampin, 2017), and because $K_{\text{Si}} = K_{\text{Se}}$ (Eq. 33),

$$\Delta G = \mu_{\text{Se}} - \mu_{\text{Si}} - \mu_m = RT \ln(K_{\text{Se}} x_{\text{Se}}) - RT \ln(K_{\text{Si}} x_{\text{Si}}) - FV_m = 0 \quad (51)$$

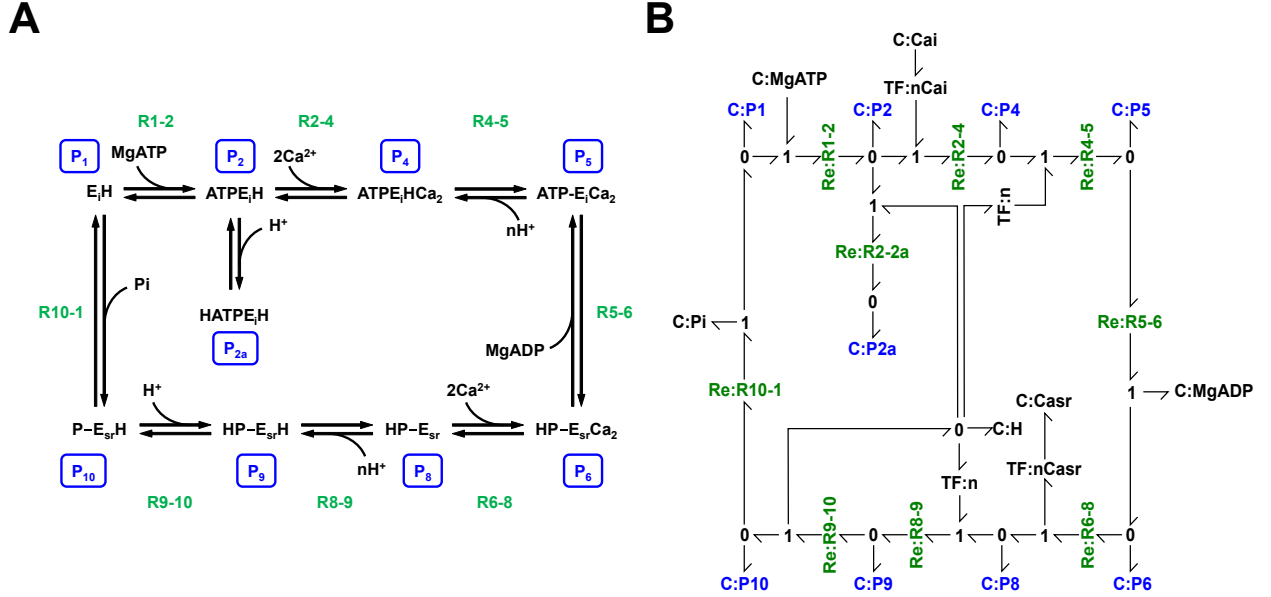


Figure 4: Kinetic and bond graph representations of the cardiac SERCA model from Tran et al. (2009). (A) Kinetic model, adapted from Fig. 2 of Tran et al. (2009). The numbers for each pump state are shown in blue boxes, and the names for each reaction are labelled in green. (B) Bond graph representation, with pump states shown in blue, and reactions in green.

the membrane potential at equilibrium is

$$V_m = \frac{RT}{F} \ln \left(\frac{x_{Se}}{x_{Si}} \right) \quad (52)$$

which is the familiar Nernst potential (Keener and Sneyd, 2009).

In Figure 3C, this system was simulated under varying membrane potentials. Because the species is positively charged, changing the membrane potential in the positive direction drives transport of the species out of the cell. The transporter achieved an equilibrium at a membrane potential of approximately 0.062, consistent with the Nernst equation in Eq. 52.

In Figure 3D we plot the Gibbs free energy (defined in Eq. 51) against membrane potential. The membrane potential has a linear contribution to the free energy of the transporter, becoming more negative for positive membrane potentials due to the positively charged substrate. Importantly, the zero of the Gibbs free energy coincides with the zero of the cycling rate in Figure 3C, thus the transporter is dissipative, and therefore thermodynamically consistent. Figure 3E shows this directly, where the transporter operates in the positive direction only if the Gibbs free energy is negative.

3. Thermodynamic models of cardiac cell transporters

3.1. SERCA

The sarcoplasmic/endoplasmic Ca²⁺ ATPase (SERCA) is an active ion transporter that pumps calcium from the cytosol into the sarcoplasmic reticulum (SR), an intracellular Ca²⁺

store, restoring the calcium released from the SR with each heart beat. Because SERCA pumps calcium against a concentration gradient ($[Ca^{2+}]_{sr} > [Ca^{2+}]_i$), it couples calcium transport to the hydrolysis of ATP in order to obtain the energy required for transport. The overall reaction of the pump is



Since the SR membrane is uncharged, the pump is driven purely by chemical energy.

SERCA has been included in a wide variety of models of cardiac cell Ca^{2+} cycling, excitation-contraction coupling and electrophysiology. Our analysis here is based on the model by [Tran et al. \(2009\)](#) which has since been incorporated into a number of subsequent cardiac cell models because it describes the dependence of cycling rate on all metabolites ([Tran et al., 2015](#); [Williams et al., 2011](#); [Walker et al., 2014](#)). The chemical reaction network and bond graph representation of the [Tran et al. \(2009\)](#) model are shown in [Figure 4](#). The structure of the bond graph closely resembles the cyclic nature of the chemical reaction scheme. However, the bond graph representation explicitly shows that the H^+ ions involved in multiple reactions are linked. Note that the bond graph representation uses **TF** components to describe multiple copies of a species in a single reaction; this is discussed further in [Appendix A](#) of the Supplementary Material.

Discussion of how bond graph parameters may be determined from an existing kinetic model are presented in [Appendix B](#) of the Supplementary Material. The kinetic parameters were thermodynamically constrained, therefore it was possible to find a set of corresponding bond graph parameters by using [Eq. B.9](#) of the Supplementary Material, with the stoichiometric matrix and resulting bond graph parameters given in [Appendix D](#). A comparison of the kinetic and bond graph models ([Figure 5A](#)) confirms that the two models match closely, with only minor discrepancies at higher cycling rates due the assumption of rapid equilibrium in the [Tran et al. \(2009\)](#) model.

SERCA accounts for approximately 10–15% of energy consumption within cardiomyocytes ([Tran et al., 2015](#); [Schramm et al., 1994](#)), and is seen as a major contributor to myocardial energy expenditure. In heart failure, SERCA activity decreases, which causes a higher proportion of Ca^{2+} to be removed via an alternative pathway – the less efficient Na^+/Ca^{2+} exchanger (NCX) – increasing energy expenditure ([Kawase and Hajjar, 2008](#)). Therefore it is important to introduce the notion of energy and efficiency into models of transporters in cardiac cells to incorporate the metabolite dependencies required for studying changes in flux under heart failure, and to compare the efficiencies of transporters that move the same substrates. While the parameters for kinetic models can be chosen such that they are thermodynamically consistent, energy-related quantities such as Gibbs free energy and power consumption do not arise naturally from these parameters. Because bond graphs explicitly model energy transfer, an advantage of using this framework is that the power consumption and efficiency are easily calculated from the model. At steady state, the Gibbs free energy of the pump can be calculated from the chemical potentials of metabolites ([Gawthrop and](#)

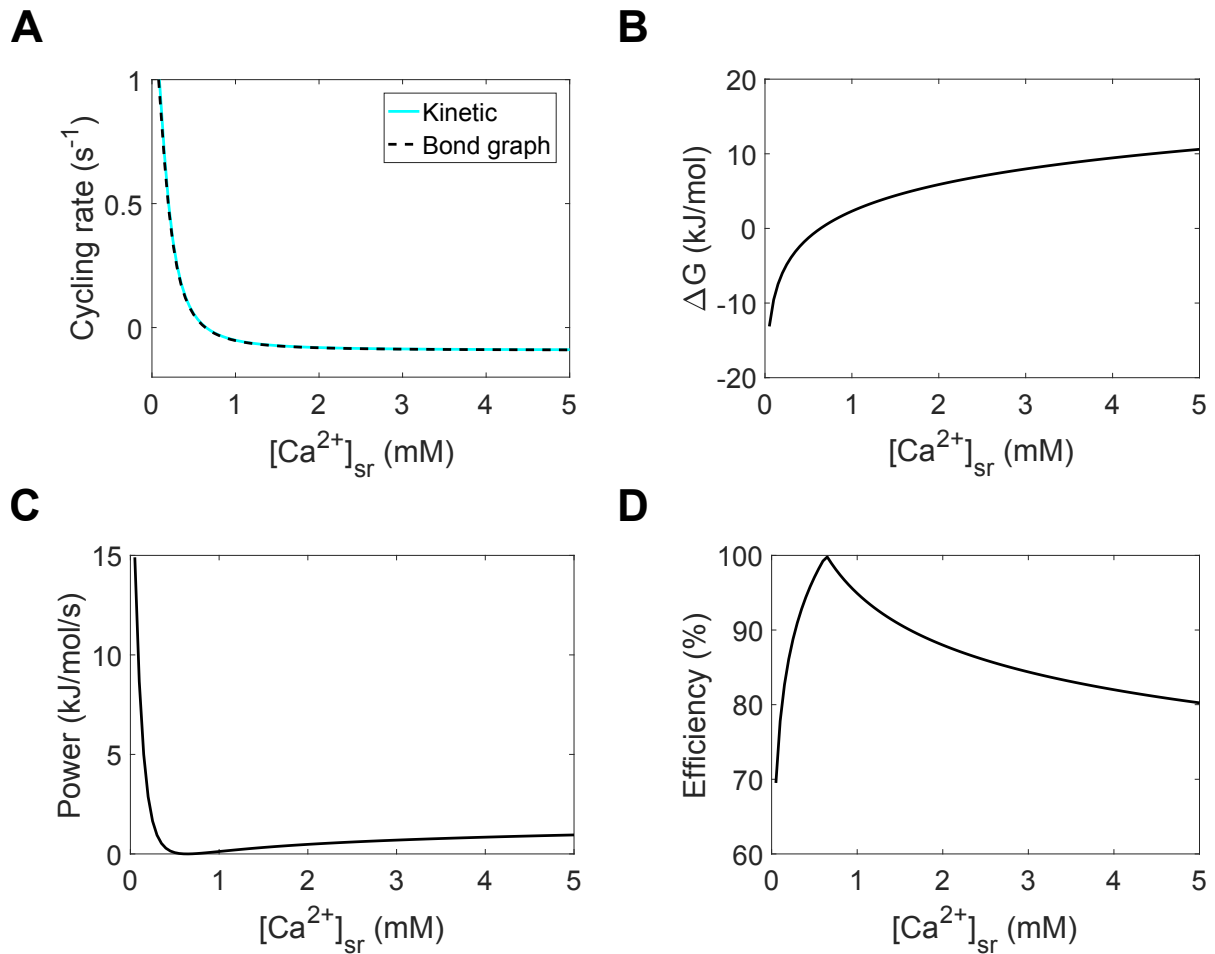


Figure 5: Simulation of the SERCA pump. (A) Comparison of cycling rates for kinetic and bond graph models, reproducing part of Fig. 13 in [Tran et al. \(2009\)](#); (B) Gibbs free energy; (C) Power consumption per mol of pump; (D) Pump efficiency. Simulations were run with $[Ca^{2+}]_i = 150$ nM, pH = 4, $[MgADP] = 0.0363$ mM, $[MgATP] = 0.1$ mM, $[Pi] = 15$ mM. Cycling rates were estimated by initialising each pump state to $1/9$ fmol, and running the simulation to its steady state.

Crampin, 2017):

$$\Delta G = 2\mu_{\text{Casr}} + \mu_{\text{MgADP}} + \mu_{\text{Pi}} + \mu_{\text{H}} - 2\mu_{\text{Cai}} - \mu_{\text{MgATP}} \quad (54)$$

The relationship between free energy and SR Ca^{2+} is shown in Figure 5B. Note that the Gibbs free energy is zero at the equilibrium point of the pump in Figure 5A, as expected of a thermodynamically consistent system. It is important to note that when $\Delta G > 0$, SERCA has been experimentally been observed to operate in the reverse direction where Ca^{2+} flows from the SR to cytosol, and ATP is synthesised (Makinose and Hasselbach, 1971). We observe in Figure 5B that a thermodynamic framework captures this reversal mode of operation, as it is a fundamental physical constraint. The product of free energy and reaction rate gives the rate of power dissipation. As seen in Figure 5C, the power consumption is positive under all conditions except at equilibrium, where it is zero.

Because the bond graph approach can split energetic contributions from different sources, it is possible to assess the efficiency of the pump. For this, we define the affinity of ATP hydrolysis as

$$A_{\text{hyd}} = \mu_{\text{MgATP}} - \mu_{\text{MgADP}} - \mu_{\text{Pi}} - \mu_{\text{H}} \quad (55)$$

and the affinity of calcium transport as

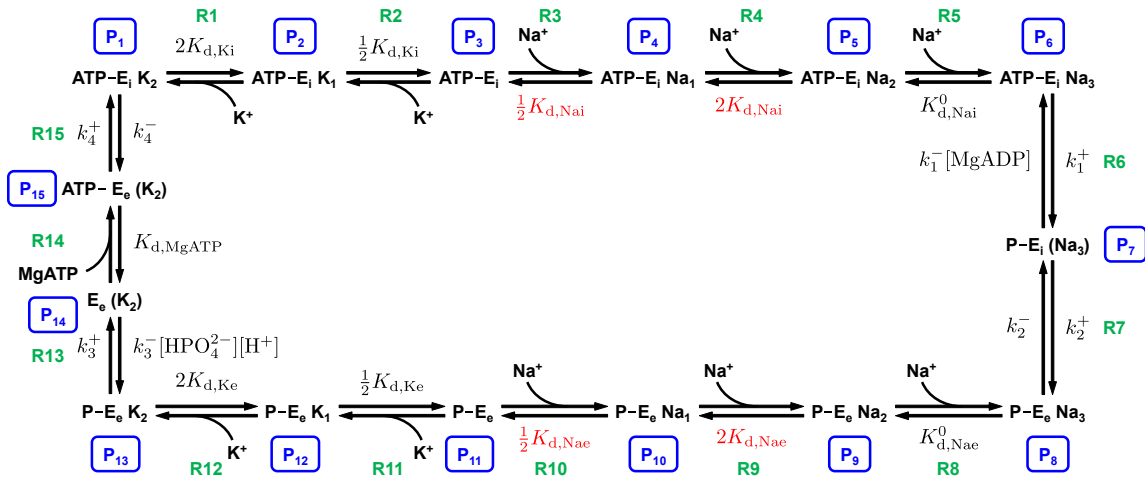
$$A_{\text{tr}} = 2\mu_{\text{Cai}} - 2\mu_{\text{Casr}} \quad (56)$$

Using the notion of pumping efficiency introduced in Gawthrop and Crampin (2018), we define the efficiency ρ as

$$\rho = \begin{cases} -A_{\text{tr}}/A_{\text{hyd}}, & A_{\text{hyd}} \geq -A_{\text{tr}} \\ -A_{\text{hyd}}/A_{\text{tr}}, & A_{\text{hyd}} < -A_{\text{tr}} \end{cases} \quad (57)$$

Thus if the pump operates in the forward direction, efficiency is the proportion of energy from ATP hydrolysis that is converted into energy for calcium transport, and if the pump operates in the reverse direction, efficiency is the proportion of energy supplied from calcium transport that is used to generate ATP. We therefore expect a cusp point at $A_{\text{hyd}} = -A_{\text{tr}}$. The efficiency of the pump is plotted in Figure 5D. This SERCA model operates reasonably efficiently under the simulated conditions, ranging from 70–100%, consistent with previous estimates that the pump is 85–90% efficient (Pinz et al., 2011). We note also a negative relationship between cycling rate and efficiency, with the pump becoming less efficient the further it moves away from equilibrium. Conversely, the pump approaches an efficiency of 100% as it nears equilibrium. However, it should be noted that in reality, SERCA pumps may exhibit “slippage”, where the pump hydrolyses ATP without transporting any Ca^{2+} (de Meis, 2002). Incorporating such behaviour into the model would likely reduce the maximum operating efficiency of the pump (Gawthrop and Crampin, 2017).

A



B

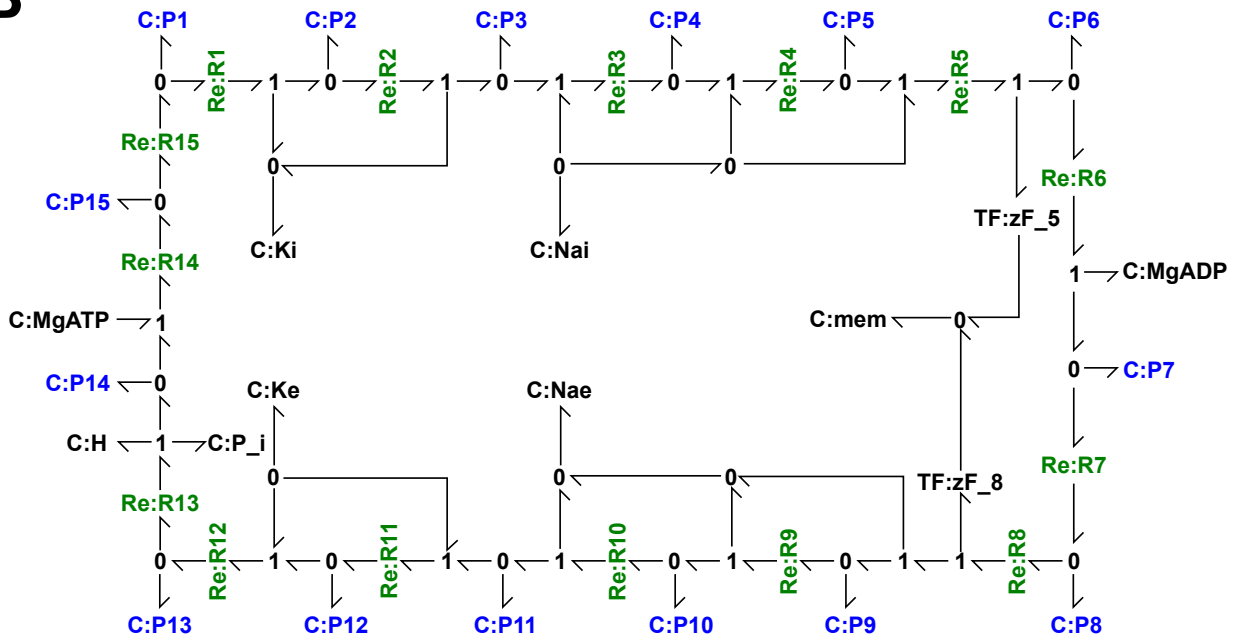


Figure 6: The cardiac Na^+/K^+ ATPase model. (A) Kinetic model, with numbers for each pump state (blue boxes) and reaction names (green) are labelled, with corrected parameters shown in red. (B) Bond graph model, with pump states coloured in blue, and reactions coloured in green.

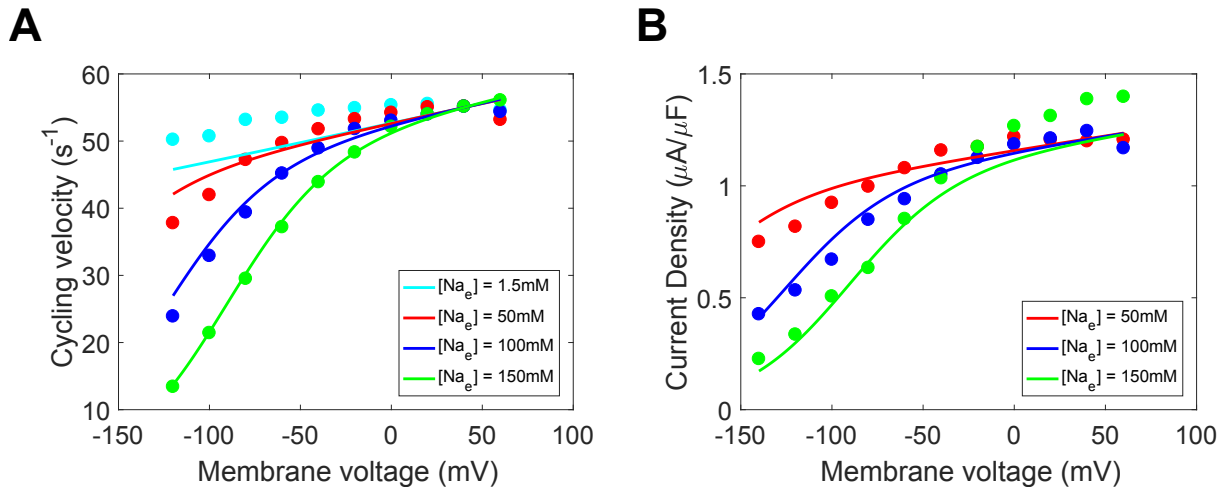
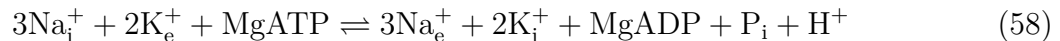


Figure 7: Fit of the cardiac Na^+/K^+ ATPase model to current-voltage measurements. (A) Comparison of the model to extracellular sodium and voltage data (Nakao and Gadsby, 1989, Fig. 3), with cycling velocities scaled to a value of 55s^{-1} at $V = 40\text{mV}$. (B) Comparison of the model to whole-cell current measurements (Nakao and Gadsby, 1989, Fig. 2A). $[\text{Na}^+]_i = 50\text{ mM}$, $[\text{K}^+]_i = 0\text{ mM}$, $[\text{K}^+]_e = 5.4\text{ mM}$, $\text{pH} = 7.4$, $[\text{Pi}]_{\text{tot}} = 0\text{ mM}$, $[\text{MgATP}] = 10\text{ mM}$, $[\text{MgADP}] = 0\text{ mM}$, $T = 310\text{ K}$.

3.2. Na^+/K^+ ATPase

The Na^+/K^+ ATPase is responsible for maintaining the Na^+ and K^+ gradients that drive ionic currents during the action potential of cardiac cells and many other excitable cells. Na^+ and K^+ are pumped against their electrochemical gradients, therefore their transport requires the supply of energy from ATP hydrolysis. The overall reaction of the pump is



In contrast to SERCA, in which only chemical potentials determine the direction of operation, the Na^+/K^+ ATPase is driven by both chemical and electrical potentials because the plasma membrane is electrically charged. Therefore a thermodynamically consistent model of Na^+/K^+ ATPase must account for both the free energy of ATP hydrolysis as well as the energetic contribution of the membrane potential.

In this section, we outline a new model of cardiac Na^+/K^+ ATPase, based on the earlier model by [Terkildsen et al. \(2007\)](#) (Figure 6). While the model of [Terkildsen et al. \(2007\)](#) is a biophysically detailed model that incorporates some thermodynamic principles, the final model is thermodynamically inconsistent. We updated the model, correcting the equilibrium constants used for identical binding sites, the equilibrium constant for ATP hydrolysis and mathematical expressions arising from the rapid equilibrium approximation, as described in Appendix C of the Supplementary Material.

We refitted the new model to the data used to parameterise the original [Terkildsen et al. \(2007\)](#) model (see Appendix C of the Supplementary Material for further detail). Comparisons of model simulations to data are given in Figures 7,8. The updated model provides a a good fit to the data, and has a comparable fit compared to the original model.

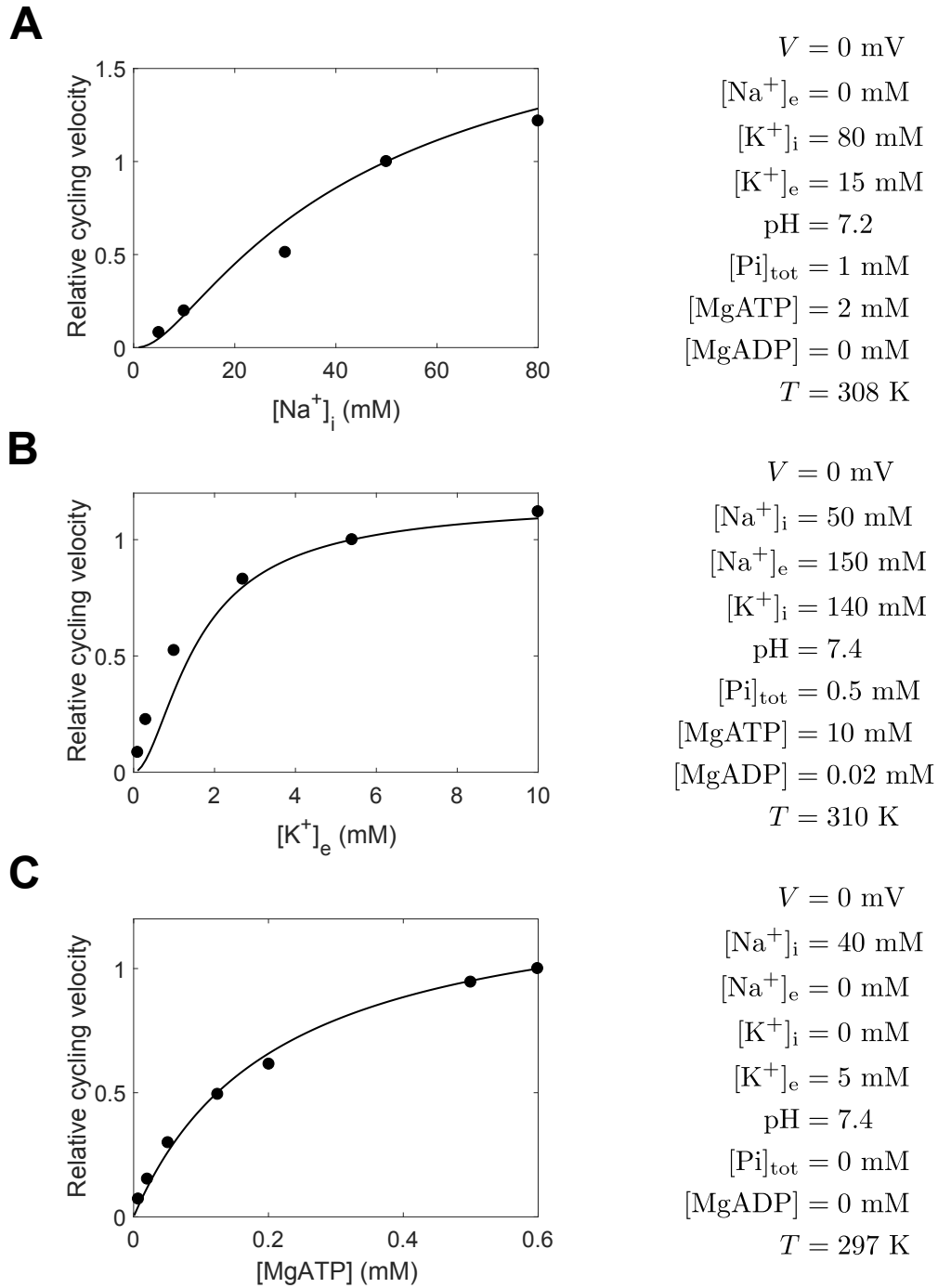


Figure 8: Fit of the cardiac Na^+/K^+ ATPase model to metabolite dependence data. Simulation conditions are displayed on the right of each figure. **(A)** Comparison of the model to data with varying intracellular sodium concentrations (Hansen et al., 2002, Fig. 7A), normalised to the cycling velocity at $[\text{Na}^+]_i = 50$ mM. **(B)** Comparison of the model to data with varying extracellular potassium (Nakao and Gadsby, 1989, Fig. 11A), normalised to the cycling velocity at $[\text{K}^+]_e = 5.4$ mM. **(C)** Comparison of the model to data with varying ATP (Friedrich et al., 1996, Fig. 3B), normalised to the cycling velocity at $[\text{MgATP}] = 0.6$ mM.

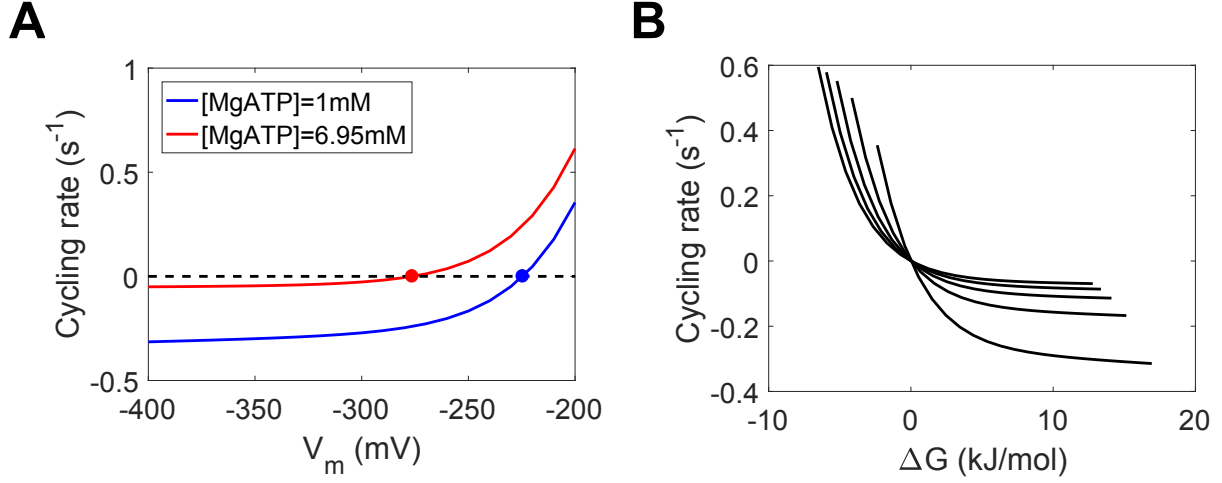


Figure 9: Simulation of the Na^+/K^+ ATPase. (A) Cycling rates of the pump near reversal potential; (B) Relationship between Gibbs free energy and cycling rate. The curves represent different concentrations of MgATP, from a concentration of 1 mM on the right, with increments of 1 mM up to a concentration of 5mM on the left. The Gibbs free energy was varied by changing the membrane potential. For (A) and (B), simulations were run using $[\text{Na}^+]_i = 10$ mM, $[\text{Na}^+]_e = 140$ mM, $[\text{K}^+]_i = 145$ mM, $[\text{K}^+]_e = 5.4$ mM, $\text{pH} = 7.095$, $[\text{Pi}] = 0.3971$ mM, $[\text{MgATP}] = 6.95$ mM, $[\text{MgADP}] = 0.035$ mM. Each pump state was initialised to $1/15$ fmol, and steady states were estimated by running each simulation to steady state.

The fit in Figure 7A was slightly worse than the original model at lower extracellular Na^+ concentrations, but the model seems to be more consistent with experimental evidence that the saturated pump velocity has little sensitivity to extracellular Na^+ at positive membrane potentials (Nakao and Gadsby, 1989).

The updated model is thermodynamically consistent, therefore it has a bond graph representation (Figure 6B). The definition of bond graph parameters and stoichiometric matrices from the fitting process are given in Appendix E of the Supplementary Material. At steady state, the Gibbs free energy of the cycle is

$$\Delta G = 3\mu_{\text{Na}^+} + 2\mu_{\text{K}^+} + \mu_{\text{MgADP}} + \mu_{\text{Pi}} + \mu_{\text{H}^+} - 3\mu_{\text{Na}^+} - 2\mu_{\text{K}^+} - \mu_{\text{MgATP}} - \mu_{\text{mem}} \quad (59)$$

$$\begin{aligned} &= \Delta G_{\text{MgATP}}^0 + RT \ln \left(\frac{[\text{MgADP}][\text{Pi}][\text{H}^+]}{[\text{MgATP}]} \right) + 3RT \ln \left(\frac{[\text{Na}^+]_e}{[\text{Na}^+]_i} \right) \\ &\quad + 2RT \ln \left(\frac{[\text{K}^+]_i}{[\text{K}^+]_e} \right) - FV_m \end{aligned} \quad (60)$$

To verify the thermodynamic consistency of the bond graph model, we simulated the steady-state operation of the pump at voltages near equilibrium, under physiological (6.95 mM) and ischaemic (1 mM) MgATP concentrations (Figure 9A). The equilibrium potentials of the pump, where cycling rates are zero, are indicated by dots. An expression for the equilibrium

potential can be derived by solving for $\Delta G = 0$:

$$V_m^{\text{eq}} = \frac{1}{F} \Delta G_{\text{MgATP}}^0 + \frac{RT}{F} \left(\ln \frac{[\text{MgADP}][\text{Pi}][\text{H}^+]}{[\text{MgATP}]} + 3 \ln \frac{[\text{Na}^+]_e}{[\text{Na}^+]_i} + 2 \ln \frac{[\text{K}^+]_i}{[\text{K}^+]_e} \right) \quad (61)$$

The predicted equilibrium potentials of -224.5 mV and -276.3 mV for $[\text{MgATP}] = 1$ mM and 6.95 mM respectively are consistent with the equilibria of the steady-state simulations, verifying thermodynamic consistency. We plotted the free energy against cycling rate for a number of MgATP concentrations, and varying the membrane potential to generate the curves in [Figure 9B](#). Despite differences in the curves, they all satisfy the fundamental constraint that $v_{\text{cyc}} = 0$ when $\Delta G = 0$, and v_{cyc} is positive only at negative free energies. Thus [Figure 9](#) verifies that the updated model is thermodynamically consistent. Like SERCA, the Na^+/K^+ ATPase is reversible, and has been experimentally observed to synthesise ATP under artificially large ionic gradients ([Glynn, 2002](#)). A thermodynamic framework is ideal for describing such phenomena.

4. Discussion

In this paper we have discussed the essential thermodynamic principles underlying membrane transporters, and how the bond graph framework captures thermodynamic constraints in these systems. We illustrated using hypothetical models that bond graphs can be used to model simple membrane transport mechanisms, incorporating relevant physical and thermodynamic constraints for both nonelectrogenic and electrogenic transport. The bond graph approach provides a single framework that naturally incorporates known thermodynamic constraints in these systems, including detailed balance ([Keener and Sneyd, 2009](#); [Liebermeister et al., 2010](#)) and the Nernst potential ([Keener and Sneyd, 2009](#)).

We applied the bond graph approach to two membrane transporters. Using the model of cardiac SERCA by [Tran et al. \(2009\)](#), we demonstrated that thermodynamically consistent models can be represented as bond graphs, and that energetic quantities are easily calculated from the bond graph model ([§ 3.1](#)). We then developed a bond graph model of cardiac Na^+/K^+ ATPase based on earlier work by [Terkildsen et al. \(2007\)](#) and [Smith and Crampin \(2004\)](#).

4.1. Thermodynamic constraints

Because bond graphs are a general-purpose modelling framework for physical systems, they unify a number of known thermodynamic constraints in the literature under a single framework, allowing thermodynamic constraints to be applied more consistently across models of biological systems. Whereas in kinetic models, Wegscheider conditions and detailed balance are used to constrain kinetic parameters in models of membrane transporters ([Keener and Sneyd, 2009](#); [Smith and Crampin, 2004](#); [Tran et al., 2009](#)), the thermodynamic parameters in a bond graph model automatically account for this constraint ([Gawthrop and Crampin, 2014](#)). In electrogenic transport, the Nernst equation ([Keener and Sneyd, 2009](#)) is a thermodynamic constraint that captures the electrochemical equilibrium. This constraint is automatically

accounted for in bond graph modelling, because the Nernst potential is automatically derived from the constitutive equations of the \mathbf{C} components for charged species, and the membrane potential (Gawthrop et al., 2017).

We believe that thermodynamically consistent models are more likely to remain robust when incorporated into whole-cell models and multi-scale models. It is often uncertain whether models remain predictive under conditions beyond the data they were parameterised on (Beattie et al., 2018; Fink et al., 2011). As discussed in Smith and Crampin (2004) and Tran et al. (2009), many existing models of transporters do not incorporate dependence for all metabolites and are therefore unable to accurately predict activity under varying metabolite concentrations. Because bond graphs enforce physical constraints on models, they provide useful constraints that dictate the behaviour of the model outside of the range of experimental data (Soh and Hatzimanikatis, 2010), being particularly useful if the experimental data were captured away from equilibrium. In order to satisfy thermodynamic consistency, bond graphs force the modeller to incorporate dependence for all metabolites in models of membrane transporters. Adherence to conservation laws may also prove important when transporter models are incorporated into multi-scale models. In models of cardiac electrophysiology, mass and charge conservation impact on long-term behaviour, and violating these conservation laws may cause the model to drift (Hund et al., 2001; Livshitz and Rudy, 2009; Pan et al., 2018a). Thus in multi-scale models where many individual submodules are simulated over time-scales far greater than they were originally developed for, accounting for conservation laws such as conservation of energy may be an important factor in maintaining the stability of these models.

4.2. Bond graph models of biological systems

In this paper, we described the representation of existing models into bond graphs, using a model of SERCA (Tran et al., 2009) as an example. These methods can be applied to a wide range existing thermodynamically consistent transporter models. A bond graph representation reveals the underlying energetics of these models (Gawthrop and Crampin, 2017). In addition to membrane transporters, models of ion channels (Gawthrop et al., 2017), redox reactions (Gawthrop, 2017), metabolic systems (Gawthrop et al., 2015) and signalling pathways (Gawthrop and Crampin, 2016) can also be represented as bond graphs. As the bond graph methodology continues to develop, we anticipate that more biological processes such as cross-bridge cycling, diffusion and gene regulation will be able to be modelled using bond graphs. Using the modularity inherent in bond graphs (Gawthrop, 2017), these models can be coupled together to assemble whole-cell models that can assess how cells deal with fundamental trade-offs between energy efficiency, speed and robustness.

While the bond graph approach can detect thermodynamic inconsistency, it is unable to detect if its thermodynamic parameters are correct. Therefore, in cases such as the model of Na^+/K^+ ATPase by Terkildsen et al. (2007), parameterising the model with incorrect species constants or equilibrium constants can lead to incorrect equilibrium points even if the model itself is internally consistent. However, we note that the bond graph framework will flag these issues to the modeller when two models with conflicting thermodynamic parameters are coupled together.

4.3. Future work

To date, a large proportion of bond graph models of biochemical systems have been derived from existing kinetic models (Gawthrop et al., 2015; Gawthrop, 2017; Gawthrop and Crampin, 2017). However, as outlined in this paper, developing new models using the bond graph framework is a more powerful approach as it guarantees thermodynamic consistency. A challenge in this process is estimating bond graph parameters from data, as kinetic information alone is insufficient to uniquely determine bond graph parameters (Gawthrop et al., 2015). Therefore future work will focus on using existing information and optimisation procedures to derive appropriate estimates of bond graph parameters from data when thermodynamic data is unavailable, and designing efficient experimental protocols for identifying bond graph parameters when thermodynamic data is available. In this process, there is a key role for quantifying the uncertainty of biological parameters (Babtie and Stumpf, 2017; Beattie et al., 2018). Given that bond graph parameters are physical quantities, it would be interesting to investigate whether these uncertainties propagate as individual models are coupled together.

We modelled transporters using multiple states with mass action equations, giving rise to steady-state velocities. However, many models of transporters are simplifications of this approach, as they are described by a single equation for the transport rate rather than multiple equations for transitions between enzyme states (Keener and Sneyd, 2009). Smith and Crampin (2004) describe a method for reducing multi-state models of membrane transporters into a single equation for transport rate by using rapid equilibrium and steady-state simplifications, while using detailed balance to ensure thermodynamic consistency. As we move towards increasingly complex multi-scale models, it is important to develop methods of simplifying models to reduce computational cost (Smith et al., 2007). An advantage of using bond graphs in the simplification process is that they impose constraints to ensure that simplified models maintain thermodynamic consistency (Gawthrop and Crampin, 2014).

5. Conclusion

We have shown that bond graphs can be used to model membrane transporters while capturing fundamental thermodynamic and physical constraints. We apply this framework to SERCA and Na^+/K^+ ATPase to develop models that are thermodynamically consistent while revealing the underlying energetics of these transporters. Combined with their inherent modularity, we believe that bond graphs are a powerful tool for incorporating models of membrane transporters into other models while maintaining thermodynamic consistency.

Data availability

The code associated with this paper is available from GitHub (https://github.com/uomsystemsbiology/transporter_thermodynamics), and is archived on Zenodo (<https://doi.org/10.5281/zenodo.1287353>) (Pan et al., 2018b). The repositories contain MATLAB code that generates the figures and CellML code containing equations for the models.

Acknowledgements

This research was in part conducted and funded by the Australian Research Council Centre of Excellence in Convergent Bio-Nano Science and Technology (project number CE140100036), and the Australian Research Council's Discovery Projects funding scheme (project DP170101358). M.P. would like to acknowledge financial support provided by an Australian Government Research Training Program Scholarship. P.J.G. would like to thank the Melbourne School of Engineering for its support via a Professorial Fellowship. K.T. is supported by the Heart Foundation of New Zealand (Research Fellowship 1692) and the Marsden Fund Council from Government funding, managed by Royal Society Te Apārangi (Marsden Fast-Start UOA1703).

References

- Anton, H., Rorres, C., 2014. Elementary linear algebra : applications version. Hoboken, NJ : John Wiley & Sons Inc.
- Atkins, P. W., De Paula, J., 2006. Physical chemistry for the life sciences. Oxford University Press ; W.H. Freeman, Oxford, UK : New York.
- Babtie, A. C., Stumpf, M. P. H., Aug. 2017. How to deal with parameters for whole-cell modelling. *Journal of The Royal Society Interface* 14 (133), 20170237. doi:10.1098/rsif.2017.0237.
- Beard, D. A., Qian, H., 2008. Chemical biophysics quantitative analysis of cellular systems. Cambridge University Press, Cambridge; New York.
- Beattie, K. A., Hill, A. P., Bardenet, R., Cui, Y., Vandenberg, J. I., Gavaghan, D. J., Boer, T. P., Mirams, G. R., Apr. 2018. Sinusoidal voltage protocols for rapid characterisation of ion channel kinetics. *The Journal of Physiology* 0 (0). doi:10.1113/JP275733.
- Blaustein, M. P., Lederer, W. J., Jul. 1999. Sodium/Calcium Exchange: Its Physiological Implications. *Physiological Reviews* 79 (3), 763–854.
- Borutzky, W., 2010. Bond Graph Methodology. Springer.
- de Meis, L., Jul. 2002. Ca²⁺-ATPases (SERCA): Energy Transduction and Heat Production in Transport ATPases. *The Journal of Membrane Biology* 188 (1), 1–9. doi:10.1007/s00232-001-0171-5.
- Fink, M., Niederer, S. A., Cherry, E. M., Fenton, F. H., Koivumäki, J. T., Seemann, G., Thul, R., Zhang, H., Sachse, F. B., Beard, D., Crampin, E. J., Smith, N. P., Jan. 2011. Cardiac cell modelling: Observations from the heart of the cardiac physiome project. *Progress in Biophysics and Molecular Biology* 104 (1–3), 2–21. doi:10.1016/j.pbiomolbio.2010.03.002.
- Friedrich, T., Bamberg, E., Nagel, G., Nov. 1996. Na⁺,K⁺-ATPase pump currents in giant excised patches activated by an ATP concentration jump. *Biophysical Journal* 71 (5), 2486–2500. doi:10.1016/S0006-3495(96)79442-0.
- Gawthrop, P., Bevan, G., Apr. 2007. Bond-graph modeling. *IEEE Control Systems* 27 (2), 24–45. doi:10.1109/MCS.2007.338279.
- Gawthrop, P., Smith, L., 1996. Metamodelling: for bond graphs and dynamic systems. Prentice Hall international series in systems and control engineering. Prentice Hall, London, New York.
- Gawthrop, P. J., Apr. 2017. Bond Graph Modeling of Chemiosmotic Biomolecular Energy Transduction. *IEEE Transactions on NanoBioscience* 16 (3), 177–188. doi:10.1109/TNB.2017.2674683.
- Gawthrop, P. J., Crampin, E. J., Nov. 2014. Energy-based analysis of biochemical cycles using bond graphs. *Proceedings of the Royal Society of London A: Mathematical, Physical and Engineering Sciences* 470 (2171), 20140459. doi:10.1098/rspa.2014.0459.
- Gawthrop, P. J., Crampin, E. J., Mar. 2016. Modular bond-graph modelling and analysis of biomolecular systems. *IET Systems Biology* doi:10.1049/iet-syb.2015.0083.
- Gawthrop, P. J., Crampin, E. J., Jun. 2017. Energy-based analysis of biomolecular pathways. *Proc. R. Soc. A* 473 (2202), 20160825. doi:10.1098/rspa.2016.0825.

- Gawthrop, P. J., Crampin, E. J., 2018. Biomolecular system energetics. In: Proceedings of the 13th International Conference on Bond Graph Modeling (ICBGM'18). Society for Computer Simulation, Bordeaux, available at arXiv:1803.09231.
- Gawthrop, P. J., Cursons, J., Crampin, E. J., Dec. 2015. Hierarchical bond graph modelling of biochemical networks. *Proc. R. Soc. A* 471 (2184), 20150642. doi:10.1098/rspa.2015.0642.
- Gawthrop, P. J., Siekmann, I., Kameneva, T., Saha, S., Ibbotson, M. R., Crampin, E. J., 2017. Bond graph modelling of chemoelectrical energy transduction. *IET Systems Biology* 11 (5), 127–138. doi:10.1049/iet-syb.2017.0006.
- Glitsch, H. G., Jan. 2001. Electrophysiology of the Sodium-Potassium-ATPase in Cardiac Cells. *Physiological Reviews* 81 (4), 1791–1826.
- Glynn, I. M., 2002. A Hundred Years of Sodium Pumping. *Annual Review of Physiology* 64 (1), 1–18. doi:10.1146/annurev.physiol.64.081501.130716.
- Guynn, R. W., Veech, R. L., Oct. 1973. The Equilibrium Constants of the Adenosine Triphosphate Hydrolysis and the Adenosine Triphosphate-Citrate Lyase Reactions. *Journal of Biological Chemistry* 248 (20), 6966–6972.
- Hansen, P. S., Buhagiar, K. A., Kong, B. Y., Clarke, R. J., Gray, D. F., Rasmussen, H. H., Nov. 2002. Dependence of $\text{Na}^+\text{-K}^+$ pump current-voltage relationship on intracellular Na^+ , K^+ , and Cs^+ in rabbit cardiac myocytes. *American Journal of Physiology - Cell Physiology* 283 (5), C1511–C1521. doi:10.1152/ajpcell.01343.2000.
- Hund, T. J., Kucera, J. P., Otani, N. F., Rudy, Y., Dec. 2001. Ionic Charge Conservation and Long-Term Steady State in the Luo–Rudy Dynamic Cell Model. *Biophysical Journal* 81 (6), 3324–3331. doi:10.1016/S0006-3495(01)75965-6.
- Hung, C.-h., Markham, T. L., 1975. The Moore-Penrose inverse of a partitioned matrix. *Linear Algebra and its Applications* 11 (1), 73–86. doi:10.1016/0024-3795(75)90118-4.
- Hwang, S.-T., Apr. 2004. Nonequilibrium thermodynamics of membrane transport. *AIChE Journal* 50 (4), 862–870. doi:10.1002/aic.10082.
- Kawase, Y., Hajjar, R. J., 2008. The cardiac sarcoplasmic/endoplasmic reticulum calcium ATPase: a potent target for cardiovascular diseases. *Nature Clinical Practice Cardiovascular Medicine* 5 (9), 554–565. doi:10.1038/npcardio1301.
- Keener, J., Sneyd, J., 2009. *Mathematical Physiology*. Vol. 8/1 of Interdisciplinary Applied Mathematics. Springer New York, New York, NY.
- Kennedy, J., Eberhart, R., Nov. 1995. Particle swarm optimization. In: *IEEE International Conference on Neural Networks*, 1995. Proceedings. Vol. 4. pp. 1942–1948 vol.4.
- Liebermeister, W., Uhlenhof, J., Klipp, E., Jun. 2010. Modular rate laws for enzymatic reactions: thermodynamics, elasticities and implementation. *Bioinformatics* 26 (12), 1528–1534. doi:10.1093/bioinformatics/btq141.
- Livshitz, L., Rudy, Y., Sep. 2009. Uniqueness and Stability of Action Potential Models during Rest, Pacing, and Conduction Using Problem-Solving Environment. *Biophysical Journal* 97 (5), 1265–1276. doi:10.1016/j.bpj.2009.05.062.
- Luo, C. H., Rudy, Y., Jun. 1994. A dynamic model of the cardiac ventricular action potential. I. Simulations of ionic currents and concentration changes. *Circulation Research* 74 (6), 1071–1096. doi:10.1161/01.RES.74.6.1071.
- Makinose, M., Hasselbach, W., 1971. ATP synthesis by the reverse of the sarcoplasmic calcium pump. *FEBS Letters* 12 (5), 271–272. doi:10.1016/0014-5793(71)80196-5.
- Mueckler, M., Thorens, B., Apr. 2013. The SLC2 (GLUT) family of membrane transporters. *Molecular Aspects of Medicine* 34 (2), 121–138. doi:10.1016/j.mam.2012.07.001.
- Nakao, M., Gadsby, D. C., Sep. 1989. [Na] and [K] dependence of the Na/K pump current-voltage relationship in guinea pig ventricular myocytes. *The Journal of General Physiology* 94 (3), 539–565. doi:10.1085/jgp.94.3.539.
- Oster, G. F., Perelson, A. S., Katchalsky, A., Feb. 1973. Network thermodynamics: dynamic modelling of biophysical systems. *Quarterly Reviews of Biophysics* 6 (01), 1–134. doi:10.1017/S0033583500000081.

- Pan, M., Gawthrop, P. J., Tran, K., Cursons, J., Crampin, E. J., 2018a. Bond graph modelling of the cardiac action potential: Implications for drift and non-unique steady states. *Proc. R. Soc. A* (In press). doi:10.1098/rspa.2018.0106.
- Pan, M., Gawthrop, P. J., Tran, K., Cursons, J., Crampin, E. J., Jun. 2018b. Supporting code for “A thermodynamic framework for modelling membrane transporters”. URL <https://zenodo.org/record/1287353#.Wx90VNUzaUk>
- Paynter, H. M., 1961. Analysis and design of engineering systems. MIT press.
- Periasamy, M., Kalyanasundaram, A., Apr. 2007. SERCA pump isoforms: Their role in calcium transport and disease. *Muscle & Nerve* 35 (4), 430–442. doi:10.1002/mus.20745.
- Pinz, I., Tian, R., Belke, D., Swanson, E., Dillmann, W., Ingwall, J. S., Mar. 2011. Compromised Myocardial Energetics in Hypertrophied Mouse Hearts Diminish the Beneficial Effect of Overexpressing SERCA2a. *Journal of Biological Chemistry* 286 (12), 10163–10168. doi:10.1074/jbc.M110.210757.
- Polettini, M., Esposito, M., Jul. 2014. Irreversible thermodynamics of open chemical networks. I. Emergent cycles and broken conservation laws. *The Journal of Chemical Physics* 141 (2), 024117. doi:10.1063/1.4886396.
- Schramm, M., Klieber, H. G., Daut, J., Dec. 1994. The energy expenditure of actomyosin-ATPase, Ca^{2+} -ATPase and Na^+ , K^+ -ATPase in guinea-pig cardiac ventricular muscle. *The Journal of Physiology* 481 (Pt 3), 647–662.
- Smith, N. P., Crampin, E. J., Jun. 2004. Development of models of active ion transport for whole-cell modelling: cardiac sodium–potassium pump as a case study. *Progress in Biophysics and Molecular Biology* 85 (2–3), 387–405. doi:10.1016/j.pbiomolbio.2004.01.010.
- Smith, N. P., Crampin, E. J., Niederer, S. A., Bassingthwaite, J. B., Beard, D. A., May 2007. Computational biology of cardiac myocytes: proposed standards for the physiome. *Journal of Experimental Biology* 210 (9), 1576–1583. doi:10.1242/jeb.000133.
- Soh, K. C., Hatzimanikatis, V., Jun. 2010. Network thermodynamics in the post-genomic era. *Current Opinion in Microbiology* 13 (3), 350–357. doi:10.1016/j.mib.2010.03.001.
- Terkildsen, J., 2006. Modelling Extracellular Potassium Accumulation in Cardiac Ischaemia. Master’s thesis, The University of Auckland.
- Terkildsen, J. R., Crampin, E. J., Smith, N. P., Nov. 2007. The balance between inactivation and activation of the Na^+ - K^+ pump underlies the triphasic accumulation of extracellular K^+ during myocardial ischemia. *American Journal of Physiology - Heart and Circulatory Physiology* 293 (5), H3036–H3045. doi:10.1152/ajpheart.00771.2007.
- Thoma, J., Bouamama, B. O., 2000. Modelling and Simulation in Thermal and Chemical Engineering. Springer Berlin Heidelberg, Berlin, Heidelberg.
- Tran, K., Loiselle, D. S., Crampin, E. J., Jul. 2015. Regulation of cardiac cellular bioenergetics: mechanisms and consequences. *Physiological Reports* 3 (7), e12464. doi:10.14814/phy2.12464.
- Tran, K., Smith, N. P., Loiselle, D. S., Crampin, E. J., Mar. 2009. A Thermodynamic Model of the Cardiac Sarcoplasmic/Endoplasmic Ca^{2+} (SERCA) Pump. *Biophysical Journal* 96 (5), 2029–2042. doi:10.1016/j.bpj.2008.11.045.
- Walker, M., Williams, G. B., Kohl, T., Lehnart, S., Jafri, M. S., Greenstein, J., Lederer, W. J., Winslow, R., Dec. 2014. Superresolution Modeling of Calcium Release in the Heart. *Biophysical Journal* 107 (12), 3018–3029. doi:10.1016/j.bpj.2014.11.003.
- Williams, G. B., Chikando, A., Tuan, H.-T. M., Sobie, E., Lederer, W. J., Jafri, M. S., Sep. 2011. Dynamics of Calcium Sparks and Calcium Leak in the Heart. *Biophysical Journal* 101 (6), 1287–1296. doi:10.1016/j.bpj.2011.07.021.

Appendix A. TF components in biochemical networks

For some reactions such as dimerisation, two or more of the same species may be involved in one side of the reaction. To represent this, the bond connected to that species is fed through a **TF** component. The **TF** component represents a transformer, which can transmit and convert energy while maintaining energy conservation. The equation for the transformer is

$$e_2 = ne_1 \quad (\text{A.1})$$

$$f_1 = nf_2 \quad (\text{A.2})$$

Where n represents the stoichiometry of the species. Since $e_1f_1 = e_2f_2$, the transformer is energy-conserving as the power in is equal to the power out of the transformer.

When applied the biochemical reaction $2A \rightleftharpoons B$, with the bond graph representation in [Figure A.1](#), the constitutive equations of the **Re** and **C** components are

$$\mu_A = RT \ln(K_A x_A) \quad (\text{A.3})$$

$$\mu_B = RT \ln(K_B x_B) \quad (\text{A.4})$$

$$v = \kappa(e^{A^f/RT} - e^{A^r/RT}) \quad (\text{A.5})$$

The equation corresponding to the transformer (with $n = 2$) is

$$A_1^f = 2\mu_A \quad (\text{A.6})$$

$$\dot{x}_A = -2v \quad (\text{A.7})$$

thus the transformer states that the rate of consumption of A is twice the rate of reaction. Because two molecules of A are consumed by the reaction, the forward affinity is twice the chemical potential of A. By combining these equations the law of mass action can be derived:

$$v = \kappa(e^{2\mu_A/RT} - e^{\mu_B/RT}) = \kappa K_A^2 x_A^2 - \kappa K_B x_B \quad (\text{A.8})$$

$$\dot{x}_A = -2v = 2\kappa K_B x_B - 2\kappa K_A^2 x_A^2 \quad (\text{A.9})$$

$$\dot{x}_B = v = \kappa K_A^2 x_A^2 - \kappa K_B x_B \quad (\text{A.10})$$

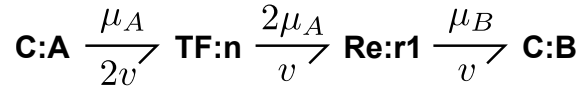
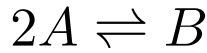


Figure A.1: Bond graph of the reaction $A \rightleftharpoons B$.

Appendix B. Converting existing kinetic models to bond graphs

Because there are a number of existing models of membrane transporters that are thermodynamically consistent, the ability to convert kinetic models of transporters into bond graphs would save a great amount of effort from having to build new bond graph models to explain existing data. In § 2.1, we outlined how a chemical reaction network can be represented as a bond graph. While the structure of the system can be naturally translated a bond graph, the parameters of existing models do not directly translate into bond graph parameters K and κ . While bond graph parameters define a unique set of kinetic parameters, identifying bond graph parameters from a set of kinetic parameters is more involved. In this section, we outline how to infer bond graph parameters from kinetic parameters, and discuss the issues that arise during this process.

We first use the enzyme cycle example in § 2.1 to illustrate the essential concepts of inferring bond graph parameters. The relationship between the kinetic and bond graph parameters is given by Eqs. 17–20. Additional constraints are enforced by the detailed balance constraint in Eq. 33. Therefore, given a set of kinetic constants k_1^+ , k_2^+ , k_1^- , k_2^- , an equivalent set of bond graph parameters can be derived by solving the Eqs. 17–20, 33. If we define \mathbf{Ln} as the element-wise logarithm operator, these constraints can be packaged into the matrix equation

$$\mathbf{Ln} \begin{bmatrix} k_1^+ \\ k_2^+ \\ k_1^- \\ k_2^- \\ 1 \end{bmatrix} = \begin{bmatrix} 1 & 0 & 1 & 0 & 1 & 0 \\ 0 & 1 & 0 & 0 & 0 & 1 \\ 1 & 0 & 0 & 0 & 0 & 1 \\ 0 & 1 & 0 & 1 & 1 & 0 \\ 0 & 0 & 1 & -1 & 0 & 0 \end{bmatrix} \mathbf{Ln} \begin{bmatrix} \kappa_1 \\ \kappa_2 \\ K_{Si} \\ K_{Se} \\ K_{E1} \\ K_{E2} \end{bmatrix} \quad (\text{B.1})$$

which can be solved through linear methods (Anton and Rorres, 2014). However, it should be noted that the rows of the right hand side are linearly dependent, as $R1+R2-R3-R4-R5 = 0$. Therefore, in order for a solution to exist, the kinetic parameters must satisfy the same dependency between rows:

$$\begin{bmatrix} 1 & 1 & -1 & -1 & -1 \end{bmatrix} \mathbf{Ln} \begin{bmatrix} k_1^+ & k_2^+ & k_1^- & k_2^- & 1 \end{bmatrix}^T = 0 \quad (\text{B.2})$$

which is easily seen to be the detailed balance constraint in Eq. 34. As a result, a set of bond graph parameters exist for this kinetic system only if the kinetic parameters are thermodynamically consistent, reflecting the fact that bond graphs can only represent the subset of kinetic systems that are thermodynamically consistent.

The equations shown above can be generalised to all chemical reaction networks described by mass action. The relationships between kinetic and bond graph parameters are captured in the general equation (Gawthrop et al., 2015)

$$\mathbf{Ln}(\mathbf{k}) = \mathbf{M}\mathbf{Ln}(\mathbf{W}\boldsymbol{\lambda}) \quad (\text{B.3})$$

with partitions defined as

$$\mathbf{k} = \begin{bmatrix} k^+ \\ k^- \\ K^c \end{bmatrix}, \quad \mathbf{M} = \left[\begin{array}{c|c} I_{n_r \times n_r} & N^f T \\ \hline I_{n_r \times n_r} & N^r T \\ \hline 0 & N^c T \end{array} \right], \quad \boldsymbol{\lambda} = \begin{bmatrix} \kappa \\ K \end{bmatrix} \quad (\text{B.4})$$

Here, k^+ and k^- are vectors of the forward and reverse kinetic rate constants respectively, $I_{n \times n}$ is an identity matrix of length n , n_r is the number of reactions, N^f and N^r are the forward and reverse stoichiometric matrices respectively, κ is a vector of the reaction rate constants, K is a vector of the species thermodynamic constants, K^c is a vector of known equilibrium constants between the species defined in the matrix N^c , and \mathbf{W} is a diagonal matrix that accounts for differences in volume between compartments. Therefore the first two rows represent the relationships between kinetic and bond graph constants, and the final row represents additional information that is known about the thermodynamic constants.

For the enzyme cycle, Eq. B.3 gives rise to Eq. B.1 through the substitutions

$$k^+ = \begin{bmatrix} k_1^+ \\ k_2^+ \end{bmatrix}, \quad k^- = \begin{bmatrix} k_1^- \\ k_2^- \end{bmatrix}, \quad \kappa = \begin{bmatrix} \kappa_1 \\ \kappa_2 \end{bmatrix}, \quad K = \begin{bmatrix} K_{Si} \\ K_{Se} \\ K_{E1} \\ K_{E2} \end{bmatrix}, \quad K^c = 1 \quad (\text{B.5})$$

$$N^f = \begin{bmatrix} 1 & 0 \\ 0 & 0 \\ 1 & 0 \\ 0 & 1 \end{bmatrix}, \quad N^r = \begin{bmatrix} 0 & 0 \\ 0 & 1 \\ 0 & 1 \\ 1 & 0 \end{bmatrix}, \quad N^c = \begin{bmatrix} 1 \\ -1 \\ 0 \\ 0 \end{bmatrix}, \quad \mathbf{W} = I_{6 \times 6} \quad (\text{B.6})$$

As seen in the enzyme cycle example, Eq. B.3 is not always solvable because there may exist sets of kinetic rate constants that do not satisfy detailed balance constraints, and are therefore thermodynamically inconsistent. Because the bond graph approach forces the modeller to use extra discipline in accounting for energy transfer, the exercise of converting kinetic parameters into bond graphs can be used to verify the thermodynamic consistency of a kinetic model. We show here that bond graph parameters can be derived from a set of kinetic parameters if they satisfy a thermodynamic constraint, known in the literature as Wegscheider conditions (Liebermeister et al., 2010). By dividing the first n_r rows of Eq. B.3 by the next n_r rows, we find that

$$\mathbf{Ln} \begin{bmatrix} K^{\text{eq}} \\ K^c \end{bmatrix} = \begin{bmatrix} -N^T \\ N^c T \end{bmatrix} \mathbf{Ln}(K) \quad (\text{B.7})$$

where $N = N^r - N^f$ is the stoichiometric matrix. If we define $/$ as the element wise quotient operator for vectors, $K^{\text{eq}} = k^+/k^-$ is a vector containing the equilibrium constants of the reactions. Thus if Z is a right nullspace matrix (Anton and Rorres, 2014) of $[-N \quad N^c]$,

multiplying both sides of Eq. B.7 by Z^T on the left gives

$$Z^T \mathbf{L} \mathbf{n} \begin{bmatrix} K^{\text{eq}} \\ K^c \end{bmatrix} = 0 \quad (\text{B.8})$$

Thus for any biochemical system with mass action equations, Eq. B.8 can be used to check that the kinetic parameters are thermodynamically consistent. As discussed in Gawthrop et al. (2015), Eq. B.8 is a form of the Wegscheider condition, which has been associated with thermodynamic consistency (Polettoni and Esposito, 2014), therefore only thermodynamically consistent kinetic parameters can be converted into bond graph parameters.

Assuming that a solution exists, one solution to Eq. B.3 can be found using the equation

$$\boldsymbol{\lambda}_0 = \mathbf{W}^{-1} \mathbf{E} \exp(\mathbf{M}^\dagger \mathbf{L} \mathbf{n}(\mathbf{k})) \quad (\text{B.9})$$

where \mathbf{M}^\dagger is the Moore-Penrose pseudoinverse of \mathbf{M} (Hung and Markham, 1975). If a solution exists, the set of bond graph parameters is generally not unique. However, as demonstrated in Gawthrop et al. (2015), the affinity and velocity each reaction remains the same regardless of the parameters chosen.

To account for differences in volume between compartments, we include a matrix \mathbf{W} in Eq. B.3. If a species exists within a compartment, the diagonal entry corresponding to that species is equal to the volume of that compartment. For reaction rate constants and species that do not exist within a volume, the value of the corresponding diagonal element is 1.

In Section 3, we use the constraints

$$\frac{W_i K_{\text{Nai}}}{W_e K_{\text{Nae}}} = 1 \quad (\text{B.10})$$

$$\frac{W_i K_{\text{Ki}}}{W_e K_{\text{Ke}}} = 1 \quad (\text{B.11})$$

$$\frac{W_i K_{\text{Cai}}}{W_{\text{sr}} K_{\text{Casr}}} = 1 \quad (\text{B.12})$$

$$\frac{W_i K_{\text{MgATP}}}{W_i K_{\text{MgADP}} W_i K_{\text{Pi}} W_{\text{isr}} K_{\text{H}}} = \exp\left(-\frac{\Delta G_{\text{MgATP}}^0}{RT}\right) \text{M}^2 = 9881 \text{ mM}^2 \quad (\text{B.13})$$

where $\Delta G_{\text{MgATP}}^0 = 11.9 \text{ kJ/mol}$ is the standard free energy of MgATP hydrolysis at 310 K (Guynn and Veech, 1973; Tran et al., 2009). We used the volumes $W_i = 38.0 \text{ pL}$, $W_e = 5.182 \text{ pL}$, and $W_{\text{sr}} = 2.28 \text{ pL}$ (Luo and Rudy, 1994). For the ATP hydrolysis reaction, we used the intracellular volume for MgATP, MgADP and Pi. In the Terkildsen et al. (2007) model, a volume of $W_{\text{isr}} = W_i$ was used for H^+ . The Tran et al. (2009) model describes the countertransport of Ca^{2+} and H^+ , however the steady-state equations were derived assuming that the cytosol and SR shared the same H^+ concentration. Therefore we chose to use the volume $W_{\text{isr}} = W_i + W_{\text{sr}}$.

In examples where charged species are involved (such as in § 2.3), the electrical dependence can be ignored for the purpose of identifying bond graph parameters, since the components

corresponding to the electrical dependence (the linear **C** component, and **TF** components) have a natural bond graph representation.

The [Tran et al. \(2009\)](#) and [Terkildsen et al. \(2007\)](#) models assumed that some reactions were at rapid equilibrium, therefore we approximated them in the bond graph model by replacing the equilibrium constants with two sufficiently fast kinetic rate constants with the same equilibrium constant.

Appendix C. Modifications to the Terkildsen et al. model of the Na⁺/K⁺ ATPase

Appendix C.1. Updates to equations

The Terkildsen *et al.* model is a 15-state model of the Na⁺/K⁺ ATPase ([Figure 6](#)). The model was reduced to a 4-state model using rapid equilibrium ([Smith and Crampin, 2004](#)), and then further simplified using steady state approximations. We found kinetic and thermodynamic issues in the implementation of this model, and resolved these issues as follows:

1. The equilibrium constants of the chemical reaction network were inconsistent with the number of binding sites. If we assume that the binding/unbinding events are identical, the kinetic rate constants are proportional to the number of binding sites ([Keener and Sneyd, 2009](#)). We have corrected the equilibrium constants, shown in red in [Figure 6A](#).
2. The original model by [Terkildsen et al. \(2007\)](#) used an incorrect standard free energy of $\Delta G_{\text{MgATP}}^0 = -30.2$ kJ/mol for the hydrolysis of ATP, which resulted in an incorrect equilibrium constant. The authors appeared to adjust $\Delta G_{\text{MgATP}}^0$ to a physiological pH rather than a pH of 0. Because $\Delta G_{\text{MgATP}}^0$ was used in the detailed balance constraint

$$\frac{k_1^+ k_2^+ k_3^+ k_4^+ K_{d,\text{Na}_e}^0 (K_{d,\text{Na}_e})^2 (K_{d,\text{K}_i})^2}{k_1^- k_2^- k_3^- k_4^- K_{d,\text{Na}_i}^0 (K_{d,\text{Na}_i})^2 (K_{d,\text{K}_e})^2 K_{d,\text{MgATP}}} = \exp\left(-\frac{\Delta G_{\text{MgATP}}^0}{RT}\right), \quad (\text{C.1})$$

the model was thermodynamically inconsistent. This error would cause over a 10⁷-fold increase in the equilibrium constant at 310 K, therefore we corrected the value to $\Delta G_{\text{MgATP}}^0 = 11.9$ kJ/mol ([Glynn and Veech, 1973](#); [Tran et al., 2009](#)).

3. [Terkildsen et al. \(2007\)](#) applied a rapid equilibrium approximation to reduce the 15-state model into a 4-state model with modified kinetic constants that were functions of metabolite concentrations. However, due to algebraic errors, the equations for some of these modified kinetic rate constants (α_1^+ , α_3^+ , α_2^- and α_4^-) were incorrect. In our updated model, we have corrected the following modified rate constants to the equations

below:

$$\alpha_1^+ = \frac{k_1^+ \tilde{N}a_{i,1} \tilde{N}a_{i,2}^2}{\tilde{N}a_{i,1} \tilde{N}a_{i,2}^2 + (1 + \tilde{N}a_{i,2})^2 + (1 + \tilde{K}_i)^2 - 1} \quad (\text{C.2})$$

$$\alpha_3^+ = \frac{k_3^+ \tilde{K}_e^2}{\tilde{N}a_{e,1} \tilde{N}a_{e,2}^2 + (1 + \tilde{N}a_{e,2})^2 + (1 + \tilde{K}_e)^2 - 1} \quad (\text{C.3})$$

$$\alpha_2^- = \frac{k_2^- \tilde{N}a_{e,1} \tilde{N}a_{e,2}^2}{\tilde{N}a_{e,1} \tilde{N}a_{e,2}^2 + (1 + \tilde{N}a_{e,2})^2 + (1 + \tilde{K}_e)^2 - 1} \quad (\text{C.4})$$

$$\alpha_4^- = \frac{k_4^- \tilde{K}_i^2}{\tilde{N}a_{i,1} \tilde{N}a_{i,2}^2 + (1 + \tilde{N}a_{i,2})^2 + (1 + \tilde{K}_i)^2 - 1} \quad (\text{C.5})$$

where

$$\tilde{N}a_{i,1} = \frac{[\text{Na}^+]_i}{K_{d,\text{Na}_i}^0 e^{\Delta FV_m/RT}} \quad \tilde{N}a_{i,2} = \frac{[\text{Na}^+]_i}{K_{d,\text{Na}_i}} \quad (\text{C.6})$$

$$\tilde{N}a_{e,1} = \frac{[\text{Na}^+]_e}{K_{d,\text{Na}_e} e^{(1+\Delta)zFV_m/RT}} \quad \tilde{N}a_{e,2} = \frac{[\text{Na}^+]_e}{K_{d,\text{Na}_e}} \quad (\text{C.7})$$

$$\tilde{K}_i = \frac{[\text{K}^+]_i}{K_{d,\text{K}_i}} \quad \tilde{K}_e = \frac{[\text{K}^+]_e}{K_{d,\text{K}_e}} \quad (\text{C.8})$$

and Δ is the charge translocated by reaction R5.

α_1^+ was one of the modified rate constants that was updated, described in [Terkildsen et al. \(2007\)](#) by the incorrect equation

$$\alpha_1^+ = \frac{k_1^+ \tilde{N}a_{i,1} \tilde{N}a_{i,2}^2}{(1 + \tilde{N}a_{i,1})(1 + \tilde{N}a_{i,2})^2 + (1 + \tilde{K}_i)^2 - 1} \quad (\text{C.9})$$

Since the modified rate constant is k_1^+ scaled by the proportion of state 6 with respect to the total amount of states 1 to 6, a correct expression for the modified rate constant can be derived as follows:

$$\begin{aligned} \alpha_1^+ &= k_1^+ \frac{x_6}{x_6 + x_5 + x_4 + x_3 + x_2 + x_1} \\ &= k_1^+ \frac{1}{1 + x_5/x_6 + x_4/x_6 + x_3/x_6 + x_2/x_6 + x_1/x_6} \\ &= \frac{k_1^+}{1 + 2\tilde{N}a_{i,1}^{-1} + 2\tilde{N}a_{i,1}^{-1}\tilde{N}a_{i,2}^{-1} + \tilde{N}a_{i,1}^{-1}\tilde{N}a_{i,2}^{-2} + 2\tilde{N}a_{i,1}^{-1}\tilde{N}a_{i,2}^{-2}\tilde{K}_i + \tilde{N}a_{i,1}^{-1}\tilde{N}a_{i,2}^{-2}\tilde{K}_i^2} \\ &= \frac{k_1^+ \tilde{N}a_{i,1} \tilde{N}a_{i,2}^2}{\tilde{N}a_{i,1} \tilde{N}a_{i,2}^2 + (1 + \tilde{N}a_{i,2})^2 + (1 + \tilde{K}_i)^2 - 1} \end{aligned} \quad (\text{C.10})$$

The mathematical expressions for the other modified rate constants can be derived using a similar procedure.

Appendix C.2. Reparameterising the Terkildsen *et al.* model

Using the updated equations of the Terkildsen *et al.* model, and setting $\Delta G_{\text{MgATP}}^0 = 11.9$ kJ/mol for the detailed balance constraint, we reparameterised the model to the same data that the Terkildsen *et al.* model was trained on. We minimised an objective function that summarised differences between model predictions and data, using similar methods to those in [Terkildsen \(2006\)](#), with some minor changes:

1. For the extracellular K^+ data of [Nakao and Gadsby \(1989\)](#) ([Figure 8B](#)), the weighting for extracellular potassium above 5.4 mM was increased from $6\times$ to $15\times$ to obtain a reasonable fit at physiological concentrations.
2. To ensure that the magnitude of cycling velocity matched that of [Nakao and Gadsby \(1989\)](#), we chose to fit the curve for $[\text{Na}^+]_e = 150$ mM ([Figure 7A](#)) without normalisation.
3. Instead of using a local optimiser to minimise the objective function, we used particle swarm optimisation ([Kennedy and Eberhart, 1995](#)) followed by a local optimiser to find a global minimum.

Appendix D. Stoichiometry and parameters for SERCA

Table D.1: Forward stoichiometric matrix for the [Tran et al. \(2009\)](#) SERCA model.

	R1→2	R2→4	R2→2a	R4→5	R5→6	R6→8	R8→9	R9→10	R10→1
P1	1	0	0	0	0	0	0	0	0
P2	0	1	1	0	0	0	0	0	0
P2a	0	0	0	0	0	0	0	0	0
P4	0	0	0	1	0	0	0	0	0
P5	0	0	0	0	1	0	0	0	0
P6	0	0	0	0	0	1	0	0	0
P8	0	0	0	0	0	0	1	0	0
P9	0	0	0	0	0	0	0	1	0
P10	0	0	0	0	0	0	0	0	1
H^+	0	0	1	0	0	0	2	0	0
Ca_i^{2+}	0	2	0	0	0	0	0	0	0
$\text{Ca}_{\text{sr}}^{2+}$	0	0	0	0	0	0	0	0	0
MgATP	1	0	0	0	0	0	0	0	0
MgADP	0	0	0	0	0	0	0	0	0
Pi	0	0	0	0	0	0	0	0	0

Table D.2: Reverse stoichiometric matrix for the [Tran et al. \(2009\)](#) SERCA model.

	R1→2	R2→4	R2→2a	R4→5	R5→6	R6→8	R8→9	R9→10	R10→1
P1	0	0	0	0	0	0	0	0	1
P2	1	0	0	0	0	0	0	0	0
P2a	0	0	1	0	0	0	0	0	0
P4	0	1	0	0	0	0	0	0	0
P5	0	0	0	1	0	0	0	0	0
P6	0	0	0	0	1	0	0	0	0
P8	0	0	0	0	0	1	0	0	0
P9	0	0	0	0	0	0	1	0	0
P10	0	0	0	0	0	0	0	1	0
H ⁺	0	0	0	2	0	0	0	1	0
Ca _i ²⁺	0	0	0	0	0	0	0	0	0
Ca _{sr} ²⁺	0	0	0	0	0	2	0	0	0
MgATP	0	0	0	0	0	0	0	0	0
MgADP	0	0	0	0	1	0	0	0	0
Pi	0	0	0	0	0	0	0	0	1

Table D.3: Parameters for the Tran SERCA model. Adapted from [Tran et al. \(2009\)](#).

Parameter	Value	Modified kinetic constants
k_1^+	$25900\text{mM}^{-1}\text{s}^{-1}$	-
k_2^+	2540s^{-1}	-
k_3^+	20.5s^{-1}	-
k_1^-	2s^{-1}	-
k_2^-	$67200\text{mM}^{-1}\text{s}^{-1}$	-
k_3^-	$149\text{mM}^{-1}\text{s}^{-1}$	-
$K_{\text{d,Cai}}^{\text{eq}}$	0.91mM	$k^+ = 3.1276 \times 10^{10}\text{mM}^{-2}\text{s}^{-1}$ $k^- = 2.5900 \times 10^{10}\text{s}^{-1}$
$K_{\text{d,Casr}}^{\text{eq}}$	2.24mM	$k^+ = 1.2996 \times 10^{11}\text{s}^{-1}$ $k^- = 2.5900 \times 10^{10}\text{mM}^{-2}\text{s}^{-1}$
$K_{\text{d,H1}}^{\text{eq}}$	$1.09 \times 10^{-5}\text{mM}$	$k^+ = 2.3761 \times 10^{15}\text{mM}^{-1}\text{s}^{-1}$ $k^- = 2.5900 \times 10^{10}\text{s}^{-1}$
$K_{\text{d,Hi}}^{\text{eq}}$	$3.54 \times 10^{-3}\text{mM}^2$	$k^+ = 2.5900 \times 10^{10}\text{s}^{-1}$ $k^- = 7.3164 \times 10^{12}\text{mM}^{-2}\text{s}^{-1}$
$K_{\text{d,Hsr}}^{\text{eq}}$	$1.05 \times 10^{-8}\text{mM}^2$	$k^+ = 2.4667 \times 10^{18}\text{mM}^{-2}\text{s}^{-1}$ $k^- = 2.5900 \times 10^{10}\text{s}^{-1}$
$K_{\text{d,H}}^{\text{eq}}$	$7.24 \times 10^{-5}\text{mM}$	$k^+ = 2.5900 \times 10^{10}\text{s}^{-1}$ $k^- = 3.5773 \times 10^{14}\text{mM}^{-1}\text{s}^{-1}$
n	2.0	-

Table D.4: Parameters for the bond graph model of the SERCA pump. The reaction parameters have unit fmol/s, and the species parameters have unit fmol⁻¹.

Species/Reaction	Parameter	Value
R1 → 2	κ_{12}	0.00053004
R2 → 4	κ_{24}	1567.7476
R2 → 2a	κ_{22a}	8326784.0537
R4 → 5	κ_{45}	1567.7476
R5 → 6	κ_{56}	3063.4006
R6 → 8	κ_{68}	130852.3839
R8 → 9	κ_{89}	11612934.8748
R9 → 10	κ_{910}	11612934.8748
R10 → 1	κ_{101}	0.049926
P ₁	K_1	5263.6085
P ₂	K_2	3803.6518
P _{2a}	K_{2a}	3110.4445
P ₄	K_4	16520516.1239
P ₅	K_5	0.82914
P ₆	K_6	993148.433
P ₈	K_8	37.7379
P ₉	K_9	2230.2717
P ₁₀	K_{10}	410.6048
H ⁺	K_H	1862.5406
Ca _i	K_{Ca_i}	1.9058
Ca _{sr}	$K_{Ca_{sr}}$	31.764
MgATP	K_{MgATP}	244.3021
MgADP	K_{MgADP}	5.8126×10^{-7}
P _i	K_{P_i}	0.014921

Appendix E. Stoichiometry and parameters for Na⁺/K⁺ ATPase

Table E.1: Forward stoichiometric matrix for the [Terkildsen et al. \(2007\)](#) model of Na⁺/K⁺ ATPase.

	Reactions														
	1	2	3	4	5	6	7	8	9	10	11	12	13	14	15
P1	1	0	0	0	0	0	0	0	0	0	0	0	0	0	0
P2	0	1	0	0	0	0	0	0	0	0	0	0	0	0	0
P3	0	0	1	0	0	0	0	0	0	0	0	0	0	0	0
P4	0	0	0	1	0	0	0	0	0	0	0	0	0	0	0
P5	0	0	0	0	1	0	0	0	0	0	0	0	0	0	0
P6	0	0	0	0	0	1	0	0	0	0	0	0	0	0	0
P7	0	0	0	0	0	0	1	0	0	0	0	0	0	0	0
P8	0	0	0	0	0	0	0	1	0	0	0	0	0	0	0
P9	0	0	0	0	0	0	0	0	1	0	0	0	0	0	0
P10	0	0	0	0	0	0	0	0	0	1	0	0	0	0	0
P11	0	0	0	0	0	0	0	0	0	0	1	0	0	0	0
P12	0	0	0	0	0	0	0	0	0	0	0	1	0	0	0
P13	0	0	0	0	0	0	0	0	0	0	0	0	1	0	0
P14	0	0	0	0	0	0	0	0	0	0	0	0	0	1	0
P15	0	0	0	0	0	0	0	0	0	0	0	0	0	0	1
K _i ⁺	0	0	0	0	0	0	0	0	0	0	0	0	0	0	0
K _e ⁺	0	0	0	0	0	0	0	0	0	0	1	1	0	0	0
Na _i ⁺	0	0	1	1	1	0	0	0	0	0	0	0	0	0	0
Na _e ⁺	0	0	0	0	0	0	0	0	0	0	0	0	0	0	0
MgATP	0	0	0	0	0	0	0	0	0	0	0	0	0	1	0
MgADP	0	0	0	0	0	0	0	0	0	0	0	0	0	0	0
Pi	0	0	0	0	0	0	0	0	0	0	0	0	0	0	0
H ⁺	0	0	0	0	0	0	0	0	0	0	0	0	0	0	0

Table E.2: Reverse stoichiometric matrix for the [Terkildsen et al. \(2007\)](#) model of Na⁺/K⁺ ATPase.

	Reactions														
	1	2	3	4	5	6	7	8	9	10	11	12	13	14	15
P1	0	0	0	0	0	0	0	0	0	0	0	0	0	0	1
P2	1	0	0	0	0	0	0	0	0	0	0	0	0	0	0
P3	0	1	0	0	0	0	0	0	0	0	0	0	0	0	0
P4	0	0	1	0	0	0	0	0	0	0	0	0	0	0	0
P5	0	0	0	1	0	0	0	0	0	0	0	0	0	0	0
P6	0	0	0	0	1	0	0	0	0	0	0	0	0	0	0
P7	0	0	0	0	0	1	0	0	0	0	0	0	0	0	0
P8	0	0	0	0	0	0	1	0	0	0	0	0	0	0	0
P9	0	0	0	0	0	0	0	1	0	0	0	0	0	0	0
P10	0	0	0	0	0	0	0	0	1	0	0	0	0	0	0
P11	0	0	0	0	0	0	0	0	0	1	0	0	0	0	0
P12	0	0	0	0	0	0	0	0	0	0	1	0	0	0	0
P13	0	0	0	0	0	0	0	0	0	0	0	1	0	0	0
P14	0	0	0	0	0	0	0	0	0	0	0	0	1	0	0
P15	0	0	0	0	0	0	0	0	0	0	0	0	0	1	0
K _i ⁺	1	1	0	0	0	0	0	0	0	0	0	0	0	0	0
K _e ⁺	0	0	0	0	0	0	0	0	0	0	0	0	0	0	0
Na _i ⁺	0	0	0	0	0	0	0	0	0	0	0	0	0	0	0
Na _e ⁺	0	0	0	0	0	0	0	1	1	1	0	0	0	0	0
MgATP	0	0	0	0	0	0	0	0	0	0	0	0	0	0	0
MgADP	0	0	0	0	0	1	0	0	0	0	0	0	0	0	0
Pi	0	0	0	0	0	0	0	0	0	0	0	0	1	0	0
H ⁺	0	0	0	0	0	0	0	0	0	0	0	0	1	0	0

Table E.3: Kinetic parameters for the updated cardiac Na⁺/K⁺ ATPase model.

Parameter	Description	Value
k_1^+	Forward rate constant of reaction R6	1423.2 s ⁻¹
k_1^-	Reverse rate constant of reaction R6	225.9048 s ⁻¹
k_2^+	Forward rate constant of reaction R7	11564.8064 s ⁻¹
k_2^-	Reverse rate constant of reaction R7	36355.3201 s ⁻¹
k_3^+	Forward rate constant of reaction R13	194.4506 s ⁻¹
k_3^-	Reverse rate constant of reaction R13	281037.2758 mM ⁻² s ⁻¹
k_4^+	Forward rate constant of reaction R15	30629.8836 s ⁻¹
k_4^-	Reverse rate constant of reaction R15	1.574 × 10 ⁶ s ⁻¹
$K_{d,Nai}^0$	Voltage-dependent dissociation constant of intracellular Na ⁺	579.7295 mM
$K_{d,Nae}^0$	Voltage-dependent dissociation constant of extracellular Na ⁺	0.034879 mM
$K_{d,Nai}$	Voltage-independent dissociation constant of intracellular Na ⁺	5.6399 mM
$K_{d,Nae}$	Voltage-independent dissociation constant of extracellular Na ⁺	10616.9377 mM
$K_{d,Ki}$	Dissociation constant of intracellular K ⁺	16794.976 mM
$K_{d,Ke}$	Dissociation constant of extracellular K ⁺	1.0817 mM
$K_{d,MgATP}$	Dissociation constant of MgATP	140.3709 mM
Δ	Charge translocated by reaction R5	-0.0550
Pump density	Number of pumps per μm^2	1360.2624 μm^{-2}

Table E.4: Parameters for the bond graph version of the updated cardiac Na^+/K^+ ATPase model.

Component	Description	Parameter	Value
R1	Reaction R1	κ_1	330.5462 fmol/s
R2	Reaction R2	κ_2	132850.9145 fmol/s
R3	Reaction R3	κ_3	200356.0223 fmol/s
R4	Reaction R4	κ_4	2238785.3951 fmol/s
R5	Reaction R5	κ_5	10787.9052 fmol/s
R6	Reaction R6	κ_6	15.3533 fmol/s
R7	Reaction R7	κ_7	2.3822 fmol/s
R8	Reaction R8	κ_8	2.2855 fmol/s
R9	Reaction R9	κ_9	1540.1349 fmol/s
R10	Reaction R10	κ_{10}	259461.6507 fmol/s
R11	Reaction R11	κ_{11}	172042.3334 fmol/s
R12	Reaction R12	κ_{12}	6646440.3909 fmol/s
R13	Reaction R13	κ_{13}	597.4136 fmol/s
R14	Reaction R14	κ_{14}	70.9823 fmol/s
R15	Reaction R15	κ_{15}	0.015489 fmol/s
P ₁	Pump state ATP-E _i K ₂	K_1	101619537.2009 fmol ⁻¹
P ₂	Pump state ATP-E _i K ₁	K_2	63209.8623 fmol ⁻¹
P ₃	Pump state ATP-E _i	K_3	157.2724 fmol ⁻¹
P ₄	Pump state ATP-E _i Na ₁	K_4	14.0748 fmol ⁻¹
P ₅	Pump state ATP-E _i Na ₂	K_5	5.0384 fmol ⁻¹
P ₆	Pump state ATP-E _i Na ₃	K_6	92.6964 fmol ⁻¹
P ₇	Pump state P-E _i (Na ₃)	K_7	4854.5924 fmol ⁻¹
P ₈	Pump state P-E _e Na ₃	K_8	15260.9786 fmol ⁻¹
P ₉	Pump state P-E _e Na ₂	K_9	13787022.8009 fmol ⁻¹
P ₁₀	Pump state P-E _e Na ₁	K_{10}	20459.5509 fmol ⁻¹
P ₁₁	Pump state P-E _e	K_{11}	121.4456 fmol ⁻¹
P ₁₂	Pump state P-E _e K ₁	K_{12}	3.1436 fmol ⁻¹
P ₁₃	Pump state P-E _e K ₂	K_{13}	0.32549 fmol ⁻¹
P ₁₄	Pump state E _e (K ₂)	K_{14}	156.3283 fmol ⁻¹
P ₁₅	Pump state ATP-E _e (K ₂)	K_{15}	1977546.8577 fmol ⁻¹
K _i	Intracellular K _i ⁺	K_{K_i}	0.0012595 fmol ⁻¹
K _e	Extracellular K _e ⁺	K_{K_e}	0.009236 fmol ⁻¹
N _{a<i>i</i>}	Intracellular Na _i ⁺	$K_{N_{a_i}}$	0.00083514 fmol ⁻¹
N _{a<i>e</i>}	Extracellular Na _e ⁺	$K_{N_{a_e}}$	0.0061242 fmol ⁻¹
MgATP	Intracellular MgATP	K_{MgATP}	2.3715 fmol ⁻¹
MgADP	Intracellular MgADP	K_{MgADP}	7.976×10^{-5} fmol ⁻¹
P _i	Free inorganic phosphate	K_{P_i}	0.04565 fmol ⁻¹
H	Intracellular H ⁺	K_H	0.04565 fmol ⁻¹
mem	Membrane capacitance	C_m	153400 fF
zF_5	Charge translocated by R5	z_5	-0.0550
zF_8	Charge translocated by R8	z_8	-0.9450